Author

Allison Pease

Title

Liquidus Determination of the Fe-S and (Fe, Ni)-S Systems at 14 and 24 GPa: Implications for the Mercurian Core

Submitted in partial fulfillment of the requirements for the degree of
Master of Science in Earth and Environmental Sciences
Department of Earth and Environmental Sciences
The University of Michigan

Accepted by:

Signature	Name	Date
Signature	Name	Date
Department Chair Signature	Name	Date

I hereby grant the University of Michigan, its heirs and assigns, the non-exclusive right to reproduce and distribute single copies of my thesis, in whole or in part, in any format. I represent and warrant to the University of Michigan that the thesis is an original work, does not infringe or violate any rights of others, and that I make these grants as the sole owner of the rights to my thesis. I understand that I will not receive royalties for any reproduction of this thesis.

☐ Permission granted.

☐ Permission granted to copy after: ________________

☐ Permission declined.

Author Signature

Earth and Environmental Sciences
University of Michigan

Table of Contents

Acknowledgments

Thank you to my advisor, Jie (Jackie) Li, for her support and guidance in conducting, presenting, and writing up this research. Thank you to Adam Simon for his suggestions and comments that improved this thesis, and thank you to Eric Hetland and Udo Becker for their preliminary comments on the manuscript. Thank you to Owen Neill for the training on the EPMA and SEM. Thank you to Jackie Wrage, Sha Chen, and Sarah Brehm, who provided excellent peer review. Thank you to Natalie Packard, Colleen Yancey, Anne Hudon, Naomi Levin, and Eric Teale, who provided valuable feedback and support throughout the project. A very special thank you to Susan and Michael Wolf; they encouraged me to complete the thesis; without them, this would not have been possible. This project was supported by: GSA (graduate research grant), COMPRES (travel grant), Tuner (research grant), Rackham (research grant), UM departmental fellowship and the NSF.

List of Tables

List of Figures

Abstract

Mercury has fascinated researchers for decades due to its sizable metallic core and weak magnetic field. The behavior of model compositions provide constraints on core conditions and regimes of solidification to predict magnetic field strength. In this study, we investigate the melting behavior of the Fe-Ni-S system, an analog composition of the Mercurian core, using a multi-anvil apparatus. We observe that the Fe-S liquidus has an inflection point at ~10 wt.% S at 14 GPa and ~11.5 wt.% S at 24 GPa, while (Fe, Ni)-S does not. At 24 GPa, Ni lowers the melting point of the Fe-S system by as much as 300°C, indicating that solidification models and adiabatic calculations must account for the presence of Ni.

Keywords: *Mercury, Fe-S, FeNi-S, liquidus, high pressure, adiabat, core, temperature*

Section 1: Introduction

The composition and structure of Mercury have been studied for decades. Ground observations revealed Mercury's high average density of 5.4 gcm^{-3}, which leads to the inference that the innermost planet possesses a sizeable metallic core covering approximately 75% of the planet's radius (Anderson et al., 1996; Riner et al., 2008). Mariner 10 was launched in 1973. Upon passing Mercury it detected a weak magnetic field. Radio-based observations of the amplitude of the planet's longitudinal librations indicate that the mantle of Mercury is decoupled from a partially molten core (Margot et al., 2007). In 2011, MESSENGER entered orbit around Mercury and determined the surface geochemistry using X-ray, gamma-ray and neutron spectrometers. MESSENGER detected an FeO-poor surface and found in the exosphere water-group ions, high abundances of Mg^{2+} and Na^+, and numerous ionized species including S^+ and H_2S^+ (Hunten and Sprague, 1997; Zurbuchen et al., 2008). The surface was found to have a high S/Si ratio (0.05-0.15), indicating the planet is rich in S.

MESSENGER provided evidence of surface geochemistry, but the chemistry of its core is still highly debated. The composition of the core is directly linked to the state, pressure, temperature, structure, and bulk composition of the planet. The pressure and temperature range of the Mercurian core are estimated to be 7-40 GPa and 1427-1727 °C, respectively (Chen et al., 2008). The lack of seismic evidence on Mercury introduces uncertainty regarding the current state and structure of the Mercurian core. Stevenson et al. (1983) pointed out that a core composed of pure Fe or Fe-Ni would be solid at the temperature-pressure conditions of the Mercurian core; therefore, the observation of a partially-fully molten core indicates the presence of light elements, which lowers the melting point of Fe. The core is predicted to be an Fe-Ni alloy with 0-5 wt.% Si and 0-10 wt.% S (Hauck et al., 2004, 2006; Malavergne et al., 2010a).

Melting experiments have been conducted on the Fe-alloy system to determine mechanisms of core solidification and provide insight into the weak magnetic field observed by MESSENGER. Terrestrial bodies, such as Earth, produce magnetic fields through the convection of a liquid Fe-alloy. The intensity of Mercury's magnetic field is a fraction of the Earth's magnetic field (Ness et al., 1974, 1975, 1976), which implies a different core state. Possible regimes of solidification include the formation of Fe, Fe_3S, Fe-S or FeSi at the core-mantle boundary, interior, or center of the core. The styles of solidification lead to unique structures for the Mercurian core: iron snow in one or more locations, the formation of an iron sulfide core, or an Fe-S shell surrounding a Si-rich outer core. Iron may precipitate out of solution at shallow depths, and iron snow may dissolve or accumulate at greater depths to form an inner core. Chen et al. (2008) predicted that given the adiabat of Mercury (11 K/GPa), iron snow could precipitate at various depths within the core. Stewart et al.

(2007) proposed the formation of an iron sulfide core for sulfur-rich compositions at pressures consistent with Mercury. Malavergne et al. (2010) predicted that an Fe-S shell would form between the core-mantle boundary and a Si-rich liquid outer core. At conditions < 15 GPa, an immiscibility gap persists between Fe-Si and Fe-S, resulting in a layered core. Iron snow and an Fe-S shell may produce a weakened magnetic field through shielding or cancellation of fields with opposite polarities (Vilim et al., 2010).

Our current knowledge of the melting behavior of Fe-alloy systems is incomplete. In particular, the shapes of the Fe-S and Fe-Ni-S liquidus curves are not well constrained at pressures >14 GPa. Studies conducted at 1 bar, 14 GPa, and 20 GPa have observed the presence of an inflection point between 8-14 wt.% S (Friedrich 1910; Miyazaki 1928; Chen et al., 2008; Pommier). Whether such an inflection point persists at higher pressures is unknown, because previous studies focused on determining the eutectic melting point and not the liquidus (Fei et al., 2000; Li et al. 2001, Stewart et al., 2007). Moreover, Ni is missing from critical experiments detailing the Fe-alloy liquidus. Nickel is a significant element in the core of Mercury. Some studies indicated that Ni did not affect the melting point of iron (Stewart et al., 2007; Pommier et al., 2018), while others observed considerable effects (Zhang et al., 2016; Boccato et al., 2017; Liu and Li, 2020; Gilfoy and Li, 2020).

In this study, we conduct multi-anvil experiments on the Fe-S system at 14 and 24 GPa to examine if the liquidus shape observed by Chen et al. (2008) persists at higher pressures. In addition, we determine if Ni lowers the melting point of the Fe-S system at 24 GPa. 14 GPa was chosen to compare experiments to Chen et al. (2008) directly. While 24 GPa was chosen because it is the highest stable pressure achievable in the University of Michigan multi-anvil apparatus, and it directly compares liquidi of different Ni concentrations at 23 GPa (Stewart et al., 2007). Other light elements

(O, N, H) were not included in this study due to the relatively small weight percent found within the core. The results from this study are applied to constrain the thermal profile of the Mercurian core.

Section 2: Experimental Methods

Melting experiments were conducted using the Walker-type multi-anvil apparatus at the University of Michigan (UM). The starting materials were mixtures of Fe (Alfa Aesar, 99.998% purity, CAS#7439-89-6, 10621), Ni (Alfa Aesar, 99.999% purity, CAS#7440-02-0, 12966), and FeS (Alfa Aesar, 99.98% purity, CAS#1317-37-9, 22388). Compositions ranging from $Fe_{99-91}S_{1-9}$, $Fe_{95-87}Ni_4S_{1-9}$, and $Fe_{87-79}Ni_{12}S_{1-9}$ (in wt.%) were mixed in an agate mortar and dried in a vacuum oven for at least 24 hours before loading.

Original and modified COMPRES 10/5 or 8/3 assemblies (Leinenweber et al., 2012) were used for 14 GPa and 24 GPa experiments, respectively (Figures 1 and 2). We conduct 24 GPa experiments with one or two samples in each experiment (Figure 2). Dual-chamber experiments allow for a simultaneous Fe-S and (Fe, Ni)-S experiment at the same pressure-temperature conditions. Single-chamber experiments at 24 GPa and some single-chamber experiments at 14 GPa included a thermocouple, and the sample was placed at the center of the cell. The double-chamber experiments at 24 GPa and some single-chamber experiments at 14 GPa did not include a thermocouple, and the temperature is inferred bases on a calibrated power curve.

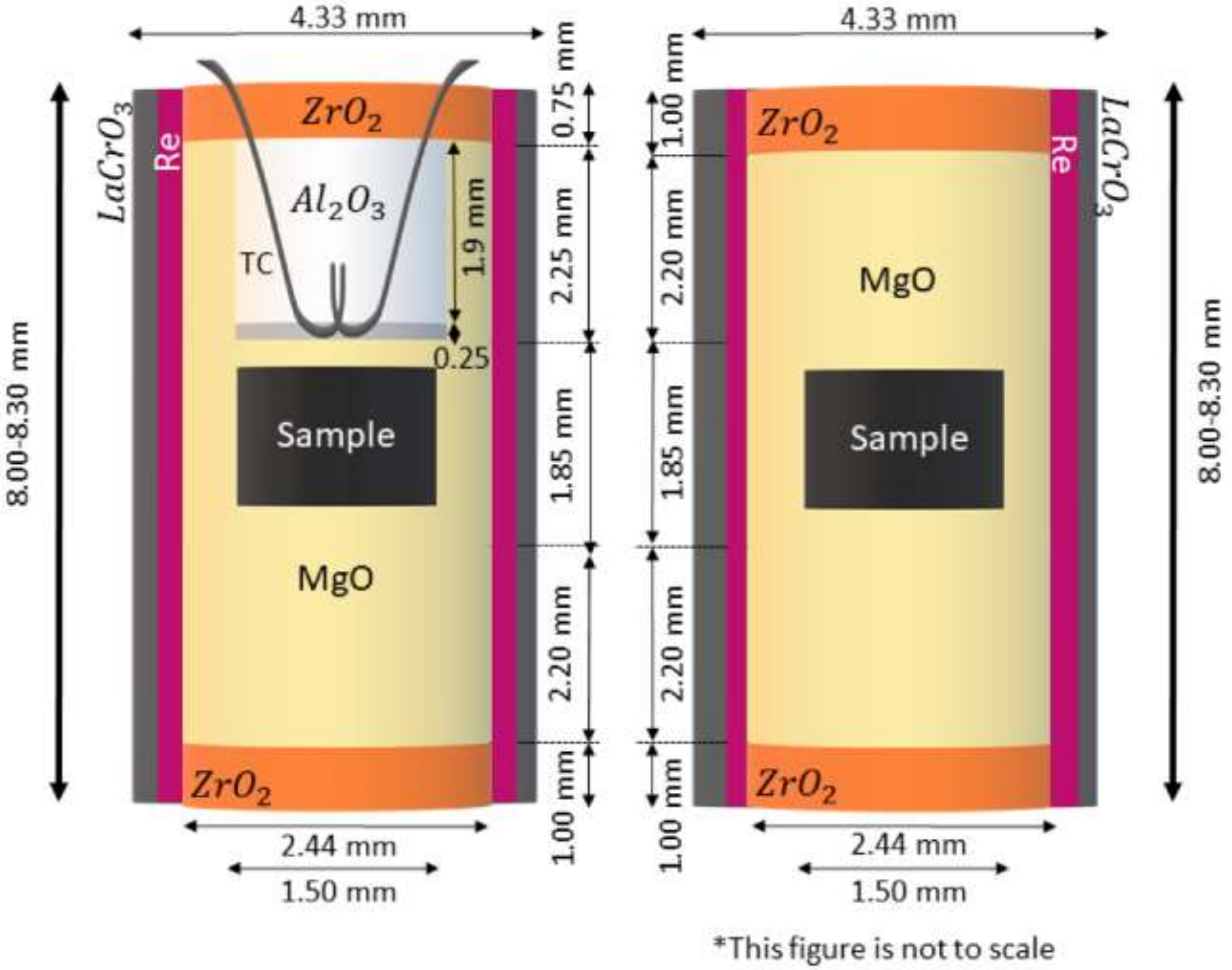

Figure 1: Configurations of 14 GPa experiments. Three experiments were conducted using the original COMPRES 10/5 assembly (left). Two experiments did not include a thermocouple (right).

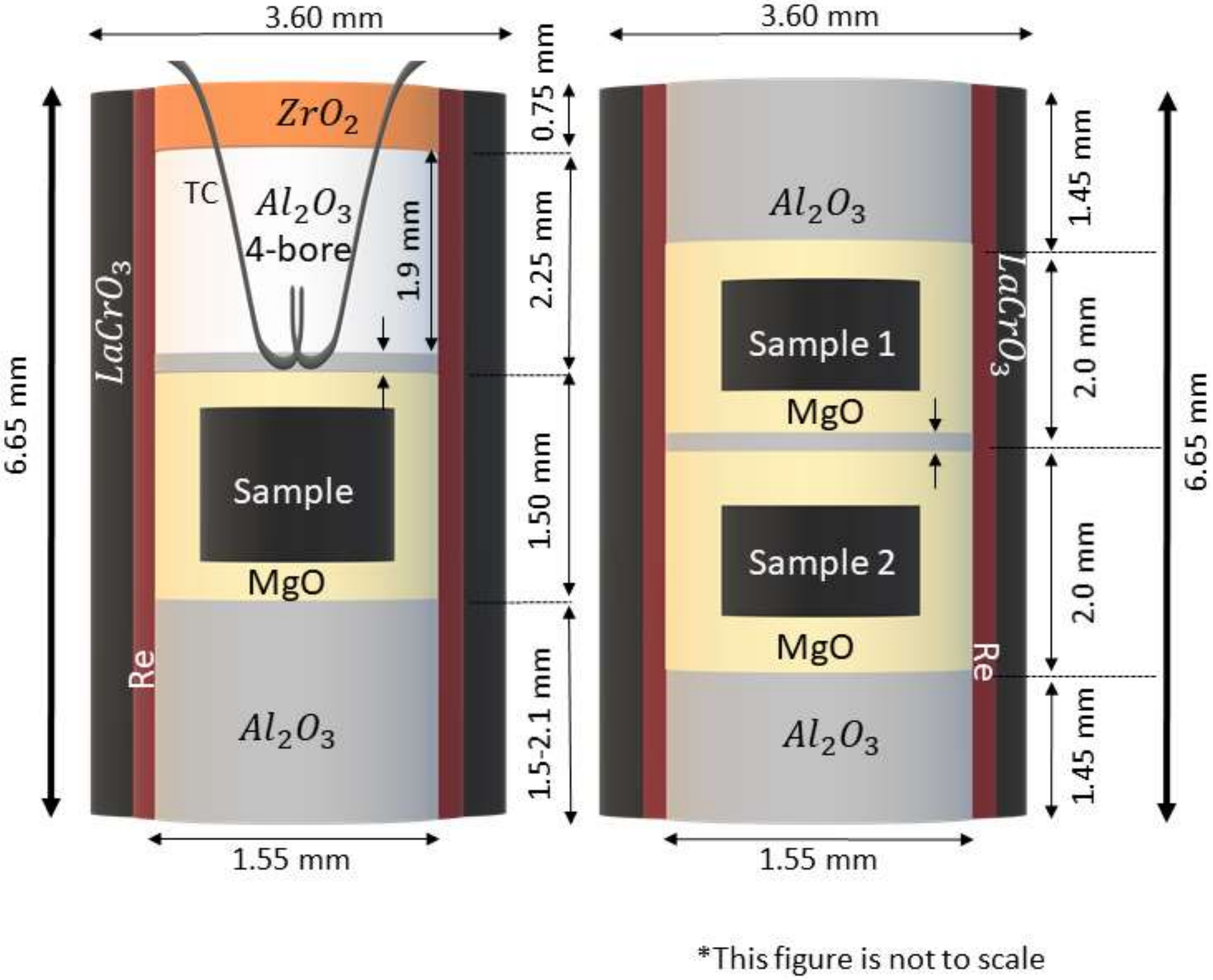

Figure 2: Configurations of 24 GPa experiments. The original COMPRES 8/3 assembly (left) was modified with a variable length of Al_2O_3. In dual-chamber experiments, the thermocouple is excluded (Right).

Once loaded into the press, the sample was brought to the target pressure of 14 GPa in 6-8 hours and to 24 GPa in 8-12 hours. Starting at 5 GPa, the sample was sintered at 600-700 °C to lower the porosity of the MgO capsule and prevent contamination between the sample and the Re-heater. When the target pressure was reached, the sample was heated at 100°C per minute to the target temperature of 1200-1900°C. All samples were held at target temperatures for 3 to 30 minutes and then rapidly (within seconds) quenched to room temperature. The recovered sample was exposed using 180, and 600 grit silicon carbide paper, and then polished using 0.3-micron Al_2O_3 powder.

Cleaned samples were carbon-coated and analyzed using a JEOL-Scanning Electron Microscope (SEM) and CAMECA SX-100 Electron Probe Micro-analyzer (EPMA) at the University of Michigan. Chalcopyrite was used as a dual standard for Fe (LIF) and S (LPET). Pure nickel was used as the Ni standard (LLIF). An accelerating potential of 20 kV and a 15 nA beam current were used with peak counting times of 10 seconds.

The compositions of the 14 GPa samples were measured using a focused beam with a four-micron step covering a 100 point EPMA grid, and using a 10-micron beam with a 10-micron step covering a 25 point EPMA grid. The compositions of the 24 GPa samples were also analyzed using a combination of a focused (<1 µm), and a defocused (10 µm) beam. The two-beam settings were compared to check validity.

Section 3: Results and Discussion

3.1 Experimental Data

Five experiments at 14 GPa yielded partially or fully molten products at 1000-1750 ˚C (Table 1, Figure 3). One experiment was on the sulfur-rich side of the eutectic. The compositions from focused and defocused-beam analyses agree within uncertainties.

Table 1 Experimental Conditions and Results on Fe-S system at 14 GPa

Experiment Name	Temp. (°C)	Time (min)	Phase	Wt.%S	Wt.% Fe	Wt.% Total	# of Points
M020419	1750 (50)	15	Solid	N/A	N/A	N/A	
			Liquid focused	1.5 (3)	99.4 (3)	101.1 (6)	99
			Liquid defocused	1.8 (6)	99.1 (6)	100.9 (8)	25
M021217	1500 (100)	15	Solid	0.18 (1)	100.6(2)	100.8 (3)	9
			Liquid focused	7.2 (7)	93.0 (7)	100.2 (9)	98
	L		Liquid defocused	8.4 (8)	91.8 (8)	100 (1)	25
M021019	1400 (50)	15	Solid	0.16 (1)	101.0 (3)	101.2 (3)	6

			Liquid focused	6.6 (7)	93.7 (8)	100 (1)	100
			Liquid defocused	6.8 (5)	93.7 (5)	100.5 (7)	25
M113016	1350 (100)	15	Solid	0.22 (3)	99.8 (3)	100 (4)	9
			Liquid focused	12.2 (5)	87.9 (5)	100.2 (7)	199
			Liquid defocused	11.9 (4)	88.4 (4)	100.3 (6)	25
M092819	1000 (50)	30	Solid	36.0	64.0	100	1*
			Liquid defocused	23.9 (3)	75.7 (3)	99.6 (4)	140

Notes: The composition was determined using both focused and defocused beams. The uncertainties in liquid compositions are standard errors of the means, and those in solid compositions are standard deviation. The notation can be read as 75.7 (3) is equal to 75.7 ± 0.3. Temperature uncertainty is estimated to be 50° when a thermocouple is used and 100˚C when a power curve is used.

*Experiment M092819 (solid) only has one composition value; the EPMA did not measure the solid phase; therefore, the composition was based on SEM/EDS measurements.

N/A indicates the sample is fully molten and there is not a coexisting solid phase

Nineteen experiments at 24 GPa yielded results between 1200 and 1900˚C (Table 2, Table 3). For the single-chamber experiments, seven were on the Fe-S system, and eight were on the (Fe, Ni)-S system. The (Fe, Ni)-S products contained 11-14 wt.% Ni. Four dual-chamber experiments produced Fe-S in one chamber and (Fe, Ni)-S with 4-5 wt.% Ni in the other.

Table 2 Experimental Conditions and Results on Fe-S system at 24 GPa

Experiment Name	Phase	Temp. (°C)	Temp. Unc (°C)	Time (min)	wt.% S	wt.% Fe	wt.% Ni	wt.% Total	# of Points
M062718	Solid	1900	100	10	0.22 (4)	99.9 (4)	N/A	100.1(4)	32
	Melt				3.4 (3)	97.0 (4)	N/A	100.4 (5)	182
M061118	Solid	1800	150	3	N/A	N/A	N/A	N/A	
	Melt				5.0 (4)	94.8 (4)	N/A	99.8 (5)	211
M083018*	Solid	1700	50	10	0.37 (4)	100.5 (3)	N/A	100.9 (3)	8
	Melt				6.7 (5)	94.0 (5)	N/A	100.7 (7)	95
M061318	Solid	1650	100	3	N/A	N/A	N/A	N/A	
	Melt				7.0 (4)	92.7 (4)	N/A	99.7 (6)	208
M071318*	Solid	1600	100	10	N/A	N/A	N/A	N/A	
	Melt				8.3 (5)	91.6 (5)	N/A	99.9 (7)	97
M060818	Solid	1500	100	3	0.7 (6)	98.7 (6)	N/A	99.4 (8)	17
	Melt				8.6 (6)	90.4 (6)	N/A	99.0 (8)	113
M062018	Solid	1550	50	5	0.54 (5)	98.6 (2)	N/A	99.1 (2)	17
	Melt				11.3 (7)	88.2 (7)	N/A	100 (1)	62
M082818*	Solid	1500	50	20	0.16 (4)	100.8 (3)	N/A	100.9 (3)	7
	Melt				12.6 (4)	86.9 (3)	N/A	99.5 (5)	153

M062518	Solid	1300	50	10	0.56 (9)	100.0 (6)	N/A	100.6 (6)	21
	Melt				14.6 (3)	85.3(5)	N/A	99.9 (6)	22
M061818	Solid	1200	100	3	0.69 (5)	98.5 (3)	N/A	99.2 (3)	44
	Melt				14.0 (2)	85.3 (2)	N/A	99.3 (3)	242
M082118*	Solid	1200	50	30	0.88 (4)	99.4 (6)	N/A	100.3 (6)	3
	Melt				14.2 (5)	87.1 (2)	N/A	100.8 (6)	24

Notes: The compositions were determined using both focused and defocused beam. The numbers in parentheses are uncertainties. Compositional uncertainties are standard deviations for solids and standard errors of the means for liquids. Temperature uncertainties are estimated on the basis distance of the thermocouple and sample chamber from the center of the cell and range from 50 to 150°.

* indicates a dual-chamber sample.

N/A indicates the sample is fully molten and there is not a coexisting solid phase.

Table 3 Experimental Conditions and Results on Fe-Ni-S system at 24 GPa

Experiment Name	Phase	Temp. (°C)	Temp. Unc (°C)	Time (min)	wt.% S	wt.% Fe	wt.% Ni	wt.% Total	# of Points
M111518	Solid	1900	100	15	0.09 (2)	87.4 (5)	13.3 (3)	100.8 (6)	9
	Melt				1.6 (5)	85.2 (8)	13.3 (2)	100 (1)	49
M111618	Solid	1750	50	10	0.15 (2)	86.6 (4)	13.91 (7)	100.7 (4)	4
	Melt				3.9 (6)	82.5 (6)	13.79 (1)	100.2 (8)	30
M083018*	Solid	1700	50	10	0.34 (4)	95.5 (3)	4.97 (1)	100.8 (3)	3
	Melt				3.8 (5)	91.6 (5)	4.74 (3)	100.1 (7)	71
M102818	Solid	1700	100	10	N/A	N/A	N/A	N/A	
	Melt				6.4 (2)	81.5 (2)	12.19 (4)	100.7 (3)	27
M111418	Solid	1600	50	15	N/A	N/A	N/A	N/A	
	Melt				5.5 (3)	82.4 (3)	12.12 (3)	100.0 (4)	38
M071318*	Solid	1600	100	10	0.24 (1)	95.8 (2)	4.7 (2)	100.7 (3)	5
	Melt				5.1 (2)	91.8 (2)	3.90(2)	100.8 (3)	35
M102618	Solid	1500	100	10	0.48 (3)	87.9 (7)	11.88 (8)	100.3 (7)	10
	Melt				8.0 (3)	81.3 (3)	11.29 (3)	100.5 (4)	26
M082818*	Solid	1500	50	20	0.3 (1)	95.2 (6)	4.96 (6)	100.5 (6)	15
	Melt				6.1 (7)	88.8 (7)	4.55 (5)	99 (1)	46
M110718	Solid	1400	50	10	0.19 (1)	87.5 (5)	12.7 (1)	100.4 (5)	10
	Melt				9.8 (2)	77.2 (3)	12.80 (3)	99.8 (3)	26
M102518	Solid	1300	50	10	0.56 (8)	89.2 (8)	11.0 (4)	100.8 (9)	4
	Melt				12.4 (7)	77.3 (9)	10.7 (1)	100 (1)	19
M110818	Solid	1200	50	20	0.3 (1)	89.6 (5)	10.9 (2)	100.8 (5)	9
	Melt				13.1 (2)	75.9 (3)	11.17 (3)	100.2 (4)	22
M082118*	Solid	1200	50	30	0.64 (3)	95.8 (7)	4.5 (6)	100.9 (9)	9

	Melt				13. 5 (2)	81.6 (2)	4.85 (7)	100.1 (3)	11

Notes: The compositions were determined using both focused and defocused beam. The numbers in parentheses are uncertainties. Compositional uncertainties are standard deviations for solids and standard errors of the means for liquids. Temperature uncertainties are estimated on the basis distance of the thermocouple and sample chamber from the center of the cell and range from 50 to 150°.

* indicates a dual-chamber sample.

N/A indicates the sample is fully molten, and there is not a coexisting solid phase.

3.2 Textual Variation

The recovered Fe-S and Fe-Ni-S liquids exhibit dendritic textures containing bright iron-rich dendrites and dark sulfur-rich matrix (Figures 3 and 4). In S-poor liquids, iron dendrites are dominant and dark matrix exists as an interstitial phase. In S-rich liquids, iron dendrites are scattered in the matrix, sometimes with a non-uniform distribution. The texture can be used to roughly estimate the sulfur content of the liquid.

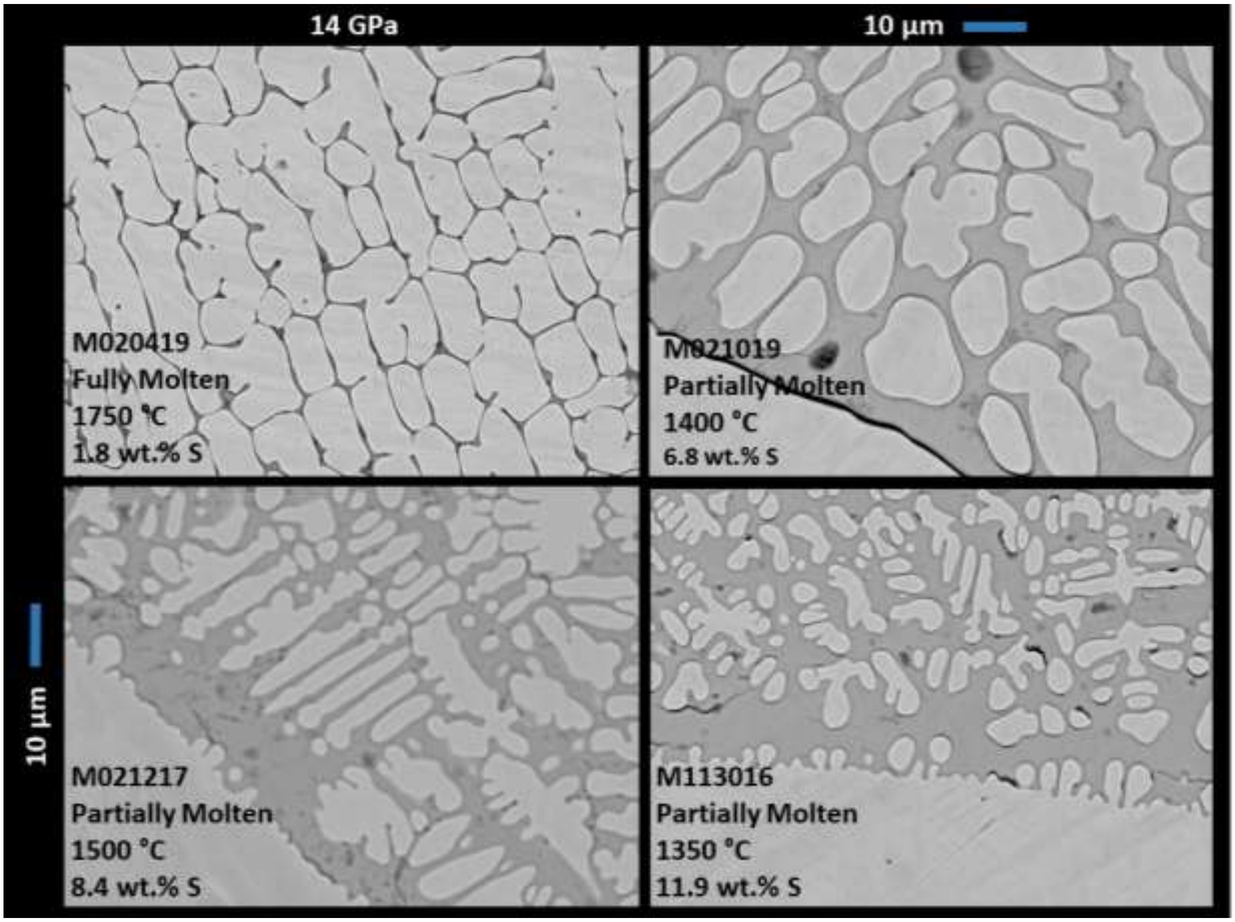

Figure 3: Backscattered electron (BSE) images of selected experiments at 14 GPa. The bright uniform region is solid iron. The region with dendritic texture was molten at high temperatures and formed an dark Fe-S matrix and bright iron dendrites when quenched.

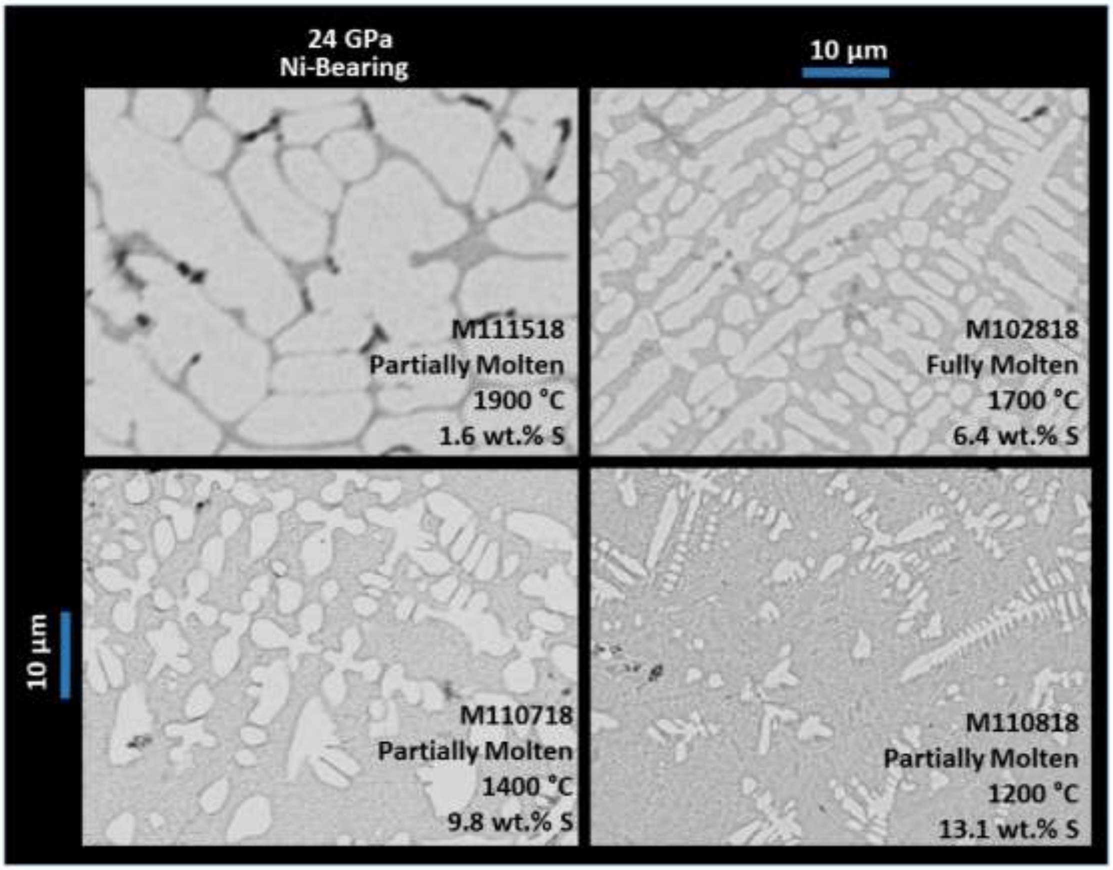

Figure 4: Backscattered electron images of representative samples from Ni-bearing experiments at 24 GPa. The region with quench texture was molten at high temperatures and formed a dark (Fe, Ni)-S matrix and bright Fe-Ni dendrites when quenched.

The Ni-free and Ni-bearing experiments showed similar trends in textural variation with temperature, as expected. In the dual-chamber experiments, it is apparent that the Ni-bearing liquid has fewer iron dendrites than the Ni-free liquid at the same pressure and temperature conditions. The Dual-chamber experiment M083018 highlights this relationship in Figure 5. This relationship implies that at the same sulfur concentration, the Ni-bearing liquidus occurs at a lower temperature than the Ni-free liquidus (Figures 7, 8, and 9).

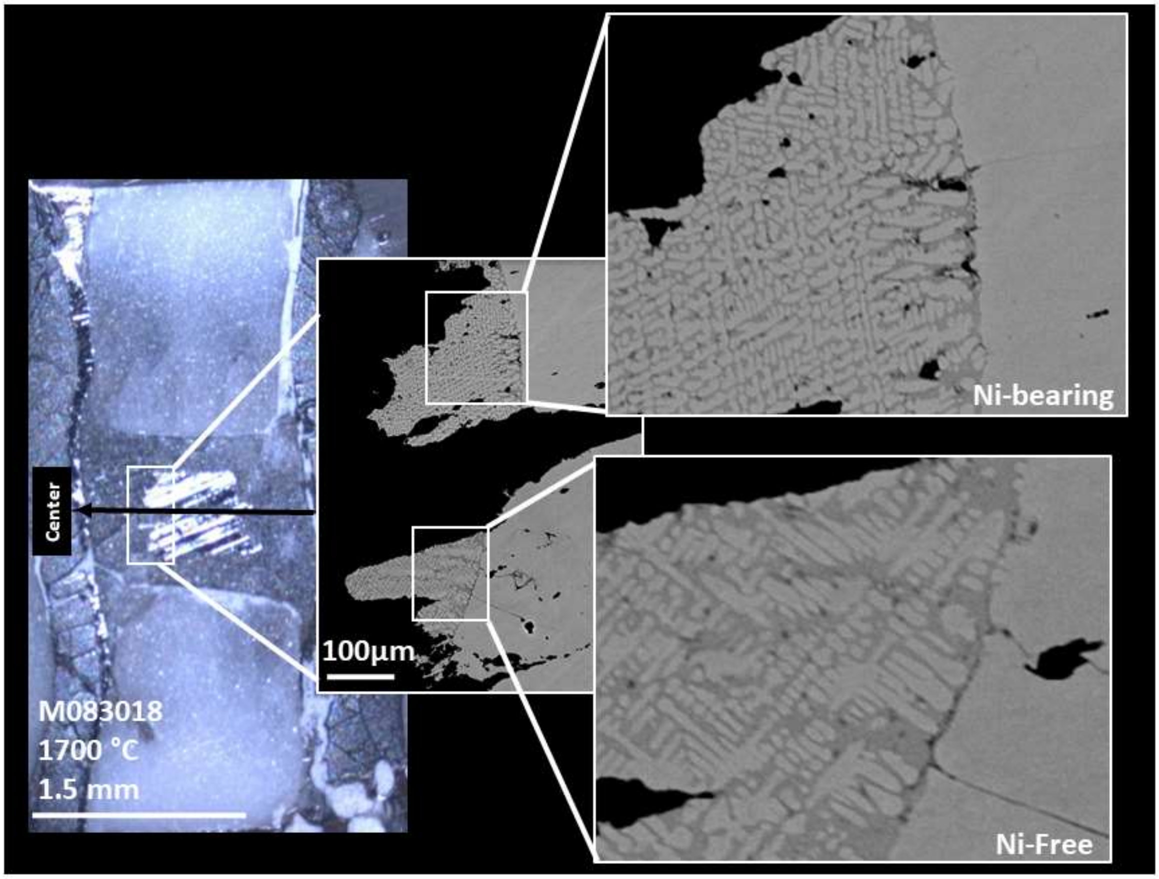

Figure 5: Configuration and product from dual-chamber experiment M083018. On the left is the optical image of the roughly polished experimental product, showing the two sample chambers in the cylindrical heater. The samples are about 50 μm apart and separated by MgO, which is denoted with an artificial black line that represents the center of the heater. The center image and right images are BSE images of (Fe, Ni)-S (upper) and Fe-S (lower).

3.3 Experimental Uncertainties in Temperature and Composition

An offset between the sample chamber and thermocouple position introduces uncertainties to the temperature measurement. The center of the chamber is the hottest region in the cell. With the 10/5 assembly, Bertka and Fei. (1997) observed a temperature spread of 100 ˚C at 1400 ° C within a sample chamber of 0.7 mm width and 0.5mm height at the center of the heater. Numerical simulations of the 8/3 assembly in Leinenweber et al. (2012) suggest that at a peak temperature of 1050 °C, the sample is isothermal within 45% of the distance from the hot center of the heater to the cold end (Figure A2). With the same approach, Hernlund et al. (2006) showed at a peak temperature of 1200°C there is a 100°C temperature reduction at 30% distance away from the center. The temperature gradients in the cell are directly related to the maximum temperature. We extrapolate this relationship for the 8/3 assembly at 1200 ˚C using Equation 1:

$$\% \text{ distance for } 100°\text{C boundary} = 3.1*10^{-5}* T(\max)^2 - 0.12*T(\max)+136 \qquad \text{[Eq. 1]}$$

This extrapolation allows us to set a criterion to accept or reject a temperature reading based on the final placements of the thermocouple junction, sample chamber, and center of the cell (Table A1). Our modified COMPRES 8/3 assemblies result in four types of products (Figure A1), depending on the lengths of Al_2O_3 end plugs and initial placements of the sample capsule and thermocouple junction. A 1.5 mm Al_2O_3 plug results in the sample and thermocouple being centered within the capsule. In comparison, 2.1 mm Al_2O_3 results in the thermocouple above the center of the capsule and the entire sample chamber within the center. Examples of acceptable final chamber conditions are shown in Figure A1. In M062718 and M102618, we infer that the thermocouple junctions are within the acceptable threshold, even though they are not fully exposed. In M061118, both the thermocouple junction and the sample are above the centerline. Although the thermocouple junction is outside the acceptable threshold, we included this experiment because the sample is fully molten, and it provides an upper bound on the liquidus.

Given the region of interest is constrained by the 100 °C uncertainty, we combined it with additional uncertainties of 25˚C that arises due to the thermocouples' random response to emf, pressure, and temperature (Li et al., 2003). The total uncertainty was reported in increments of 50˚C.

For uncertainties in compositions, the standard error of the mean is used when the sample region is heterogeneous, and the beam size is too small to capture both dendrites and matrix with their average portions in the liquid. Standard deviation is used for homogenous solid phase and broad-beam analyses to report the spread in data measurements. The Ni concentrations in the matrix and dendrites are similar, the standard errors of the means give exceedingly small uncertainties in the Ni contents of the liquids. The actual uncertainties in the Ni contents are more consistent with standard deviation on the order of 0.3 rather than an average of 0.05 reported as the standard errors of the means.

3.4 Liquidus Curve at 14 GPa

Five experiments yielded constraints on the Fe-S liquidus curve at 14 GPa (Table 1, Figure 6). Together with experimental results from Chen et al. (2008), Anzellini et al. (2013), and Boehler (1993) the 14 GPa liquidus on the iron-rich side of the eutectic was fitted using a fourth-order polynomial in the form of $T\ (^{\circ}C) = K_0+K_1*x+K_2*x^2+K_3*x^3$ with an R^2 value of 0.9981. Coefficient values ± one standard deviation: $K_0=1910 \pm 40$, $K_1=-150 \pm 25$, $K_2=16\pm3$, $K_3= -0.6 \pm 0.1$. Our data confirm that an inflection point exists on the iron-rich side of the eutectic at ~10 wt.% sulfur. Experiment M092819 provides the first constraint on the liquidus curve on the sulfur-rich side of the eutectic, suggesting that it is considerably lower than the liquidus proposed by Fei et al. (2001).

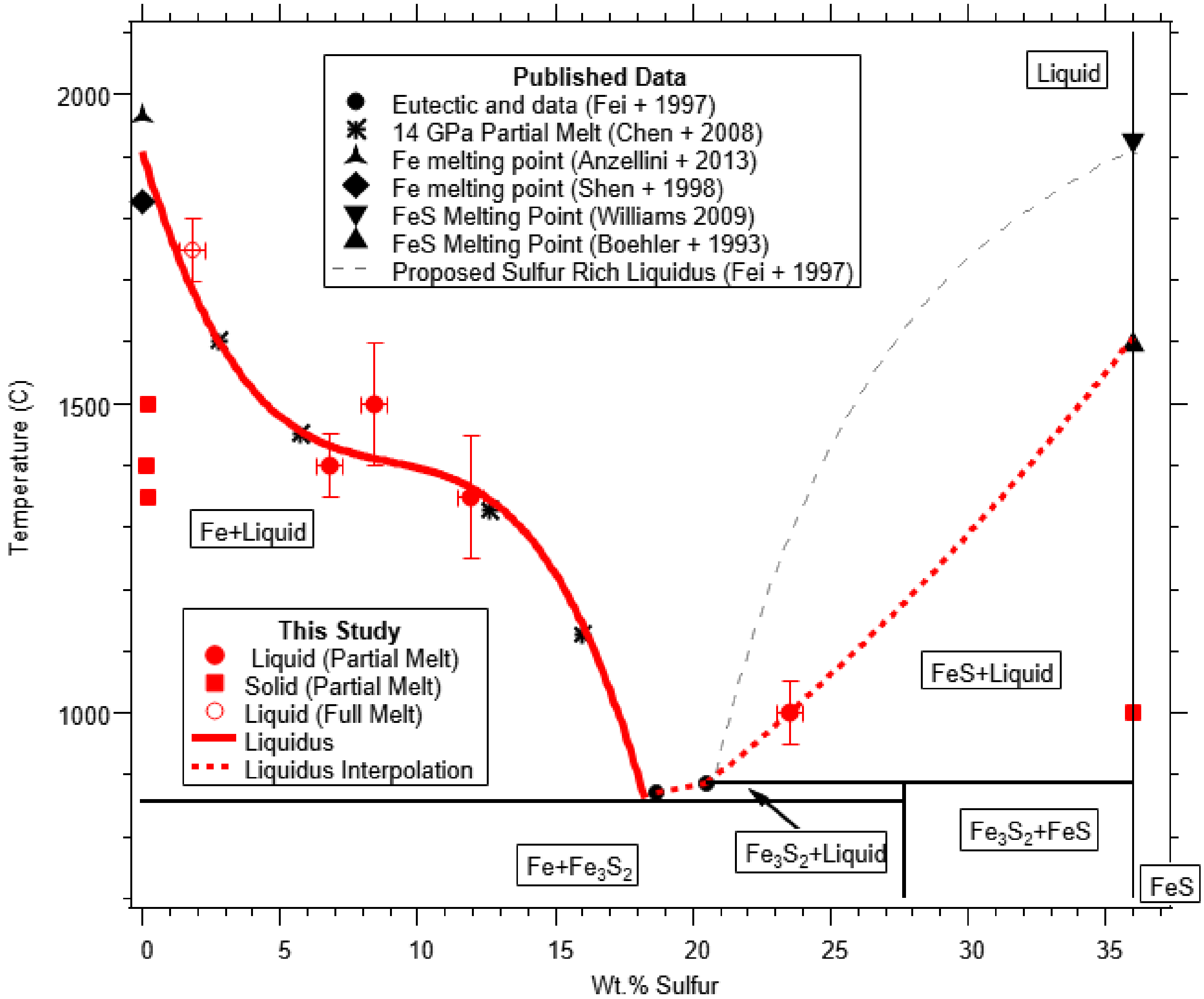

Figure 6: Fe-S liquidus at 14 GPa. The liquidus curve for the iron-rich side of the eutectic (red solid curve) is based on experimental data from this study (the red solid squares and circles represent coexisting solids and melts, respectively, while the open circles represent stand-alone melts) and published data (stars from Chen et al. (2008)), the solid circles for the eutectic and peritectic points from Fei et al. (1997). Melting point of iron is from Shen et al. (1998) and Anzellini et al.(2013). The dashed liquidus curve on the sulfur-rich side of the eutectic is drawn through the data point from this study and the melting point of FeS (Boehler, 1993; Fei et al. (1997); Williams, 2009).

3.5 Liquidus Curves at 24 GPa

3.5.1 From Single Chamber Experiments

Nineteen experiments at 24 GPa yielded constraints on the Fe-S and (Fe, Ni)-S liquidus curves (Table 2 and 3). Seven single-chamber experiments on the Fe-S system, five partially molten and two fully molten, suggest the presence of an inflection point at ~ 11.5 wt.% S (Figure 7). The experiment at 1550 ˚C (M062018) provides a critical constraint. It contains a small amount of melt, and therefore the probe measurements cannot capture the overall melt composition accurately. To better constrain the melt composition, we conducted a spatial analysis of the melt region using ImageJ to determine the relative proportions of the dendrites and matrix. The composition was then calculated from the proportions and the compositions of the dendrites and matrix determined using a focused beam. The calculated sulfur content is 9.8 wt.% sulfur in one region and 14.2 wt.% in another region. Each region takes up about half of the exposed sample chamber. By weighting the two regions equally, the approximate composition is 12 wt.% sulfur. We report the 9.8-14.2 wt.% S to reflect the large uncertainties (Figure 7). This estimate agrees with the probe result of 11.3 (7) wt.% S and indicates the presence of an inflection point in the liquidus curve.

Eight single-chamber experiments on the (Fe, Ni)-S system, six partially molten and two fully molten, suggest that the (Fe, Ni)-S liquidus curve for 11-14 wt.% Ni is located at lower temperatures than the Fe-S liquidus, and does not contain an inflection point. The curve is slightly concaved upwards. The location and shape are consistent with the results of Gilfoy and Li (2020) at 20 GPa.

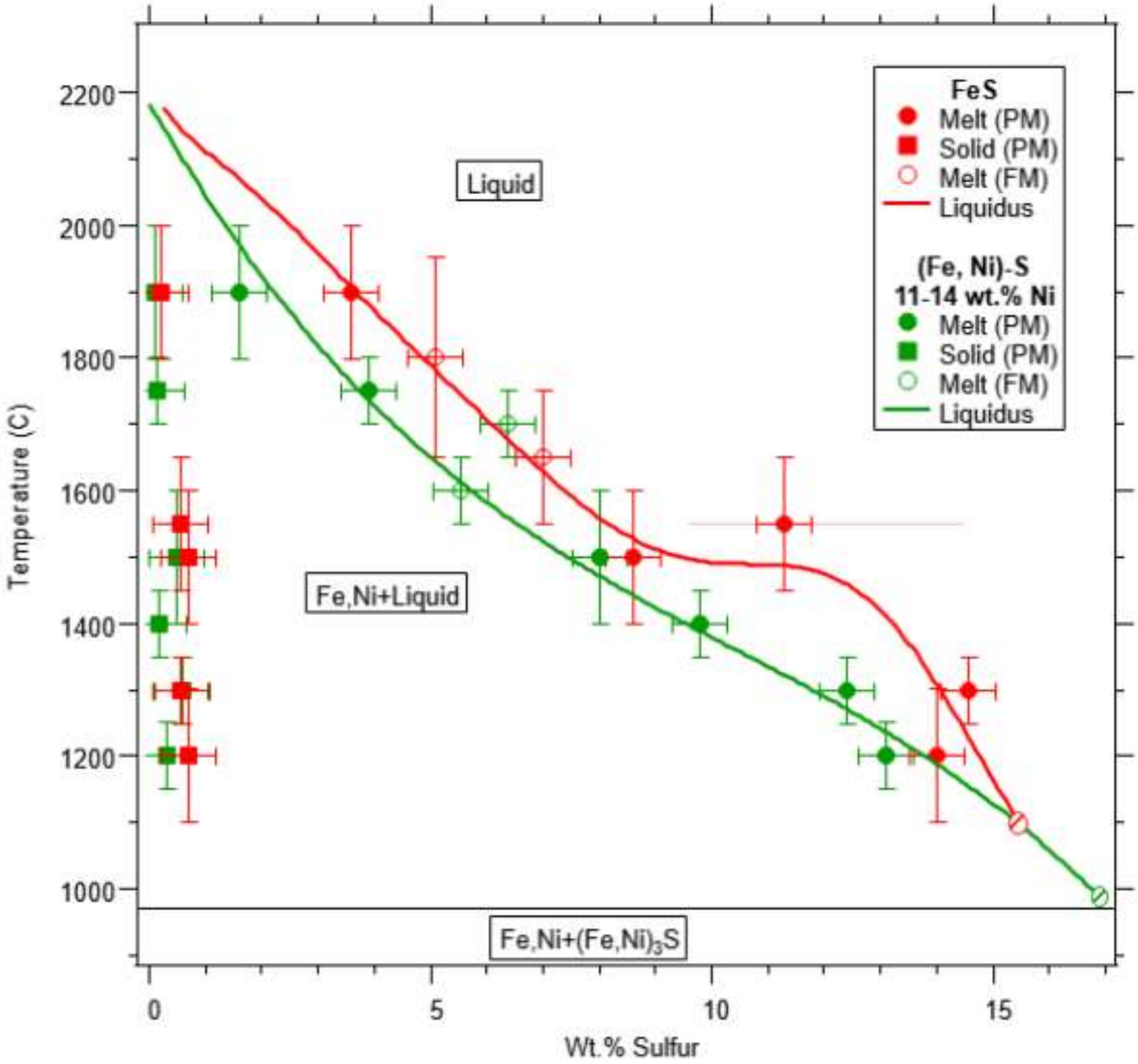

Figure 7 Fe-S and (Fe, Ni)-S (11-14 wt.%Ni) liquidus curves from single-chamber experiments at 24 GPa. The red and green curves, respectively. The solid squares and circles represent the coexisting solid and liquid phase, respectively, while the open circles represent stand-alone melts. The eutectic point is at the hatched circle and is approximated based on Li et al. (2001), Stewart et al. (2007) and Zhang and Fei (2008). The melting point of iron is calculated according to the fitted curve in Anzellini et al. (2013) and Boccato et al. (2017).

3.5.2 From Dual-Chamber Experiments

The four dual-chamber experiments at 24 GPa provide a direct comparison between the Ni-free and Ni-bearing Fe-S liquidus curves. The nickel concentration, in this set of experiments, ranged from 4-5 wt.%. The (Fe, Ni)-S liquidus is at lower temperatures than the Fe-S liquidus (Figure 8). The inflection point of the Fe-S system and its absence in the (Fe, Ni)-S system are confirmed.

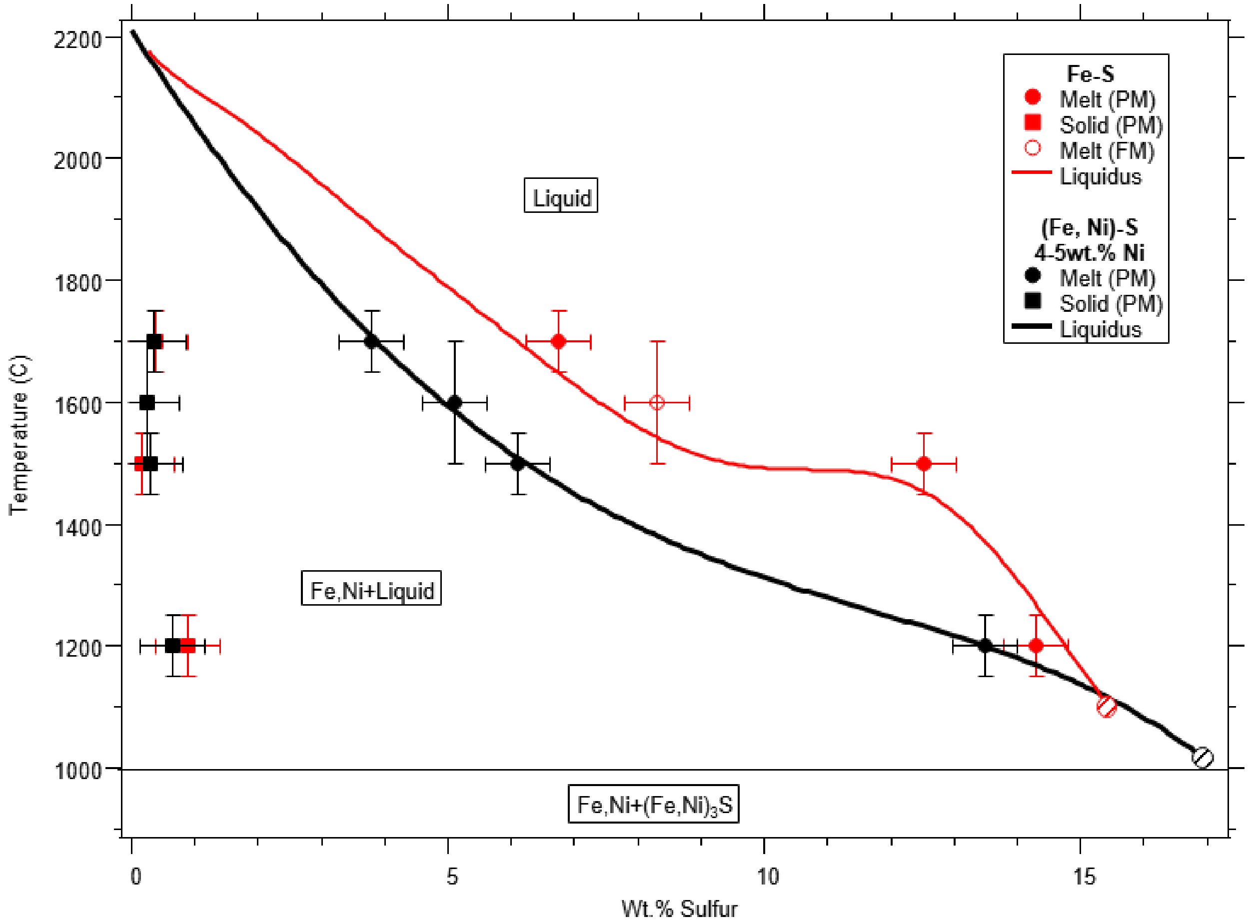

Figure 8: Fe-S and (Fe, Ni)-S (4.5 wt.%Ni) liquidus curves at 24 GPa from dual-chamber experiments. The solid squares and circles represent the coexisting solid and liquid, and the open circles represent stand-alone liquidus. The eutectic is approximated, and the value is interfered from Li et al. (2001), Stewart et al. (2007) and Zhang and Fei (2008). The melting point of iron calculated form Anzellini et al. (2013) and Boccato et al. (2017).

3.6 Comparison to Published Data

3.6.1 Eutectic point and Fe-Ni melting point.

The Fe-S eutectic point has been determined at a range of pressures (Figure A3). In general, as the pressure increases, the eutectic shifts to a lower sulfur concentration. The eutectic temperature decreases with pressure between 1 bar and 15 GPa, and then increases with pressure (Li and Fei 2014). The eutectic composition at 24 GPa is interpolated between those at 23 GPa (Stewart et al.,

2007) and 25 GPa (Li et al., 2001). The melting point of Fe at 24 GPa is calculated from the curve proposed by Anzellini et al. (2013), and it is ~150 °C higher than the melting point of Fe shown in Stewart et al. (2007).

The (Fe, Ni)-S eutectic has been partially constrained at a range of pressures. Stewart et al. (2007) determined the eutectic points of (Fe, Ni)-S system containing 36 wt.% Ni at 23 and 40 GPa. They did not examine how the concentration of Ni affected the (Fe, Ni)-S eutectic composition and temperature. Zhang and Fei (2008) observed that the temperature of the eutectic point decreases with increasing Ni content. We estimated the eutectic points of (Fe, Ni)-S systems at 24 GPa containing 4-5 wt.% Ni to be 16.8 wt.% S and 1020°C; 11-14 wt.% Ni to be 17 wt.% S and 980°C, shown in Figures 7, 8, and 9, as hatched circles (Stewart et al., 2007; Zhang and Fei, 2008). A recent study suggests that the melting point of Fe-Ni is higher than that of pure iron by 2 ˚C/wt.% Ni (Boccato et al., 2017). Accordingly, we estimated the melting point of Fe-Ni with 11-14 wt.% Ni and 4-5 wt.% Ni to be 2224°C and 2210°C, respectively.

3.6.2 Fe-S liquidus at 1 bar to 40 GPa

At 1 bar, the Fe-S liquidus has an inflection point, which vanishes at elevated pressures (Buono et al., 2013), and then reappears at 14 GPa (Chen 2008) and persists at 20 GPa (Pommier et al. 2018). Our Fe-S experiments at 24 GPa confirm the presence of an inflection point in the liquidus curve, contrary to the concave-downward curves proposed by Stewart (2007). We note that the actual data points of Stewart et al. (2007) are consistent with the fitted liquidus curve in this study.

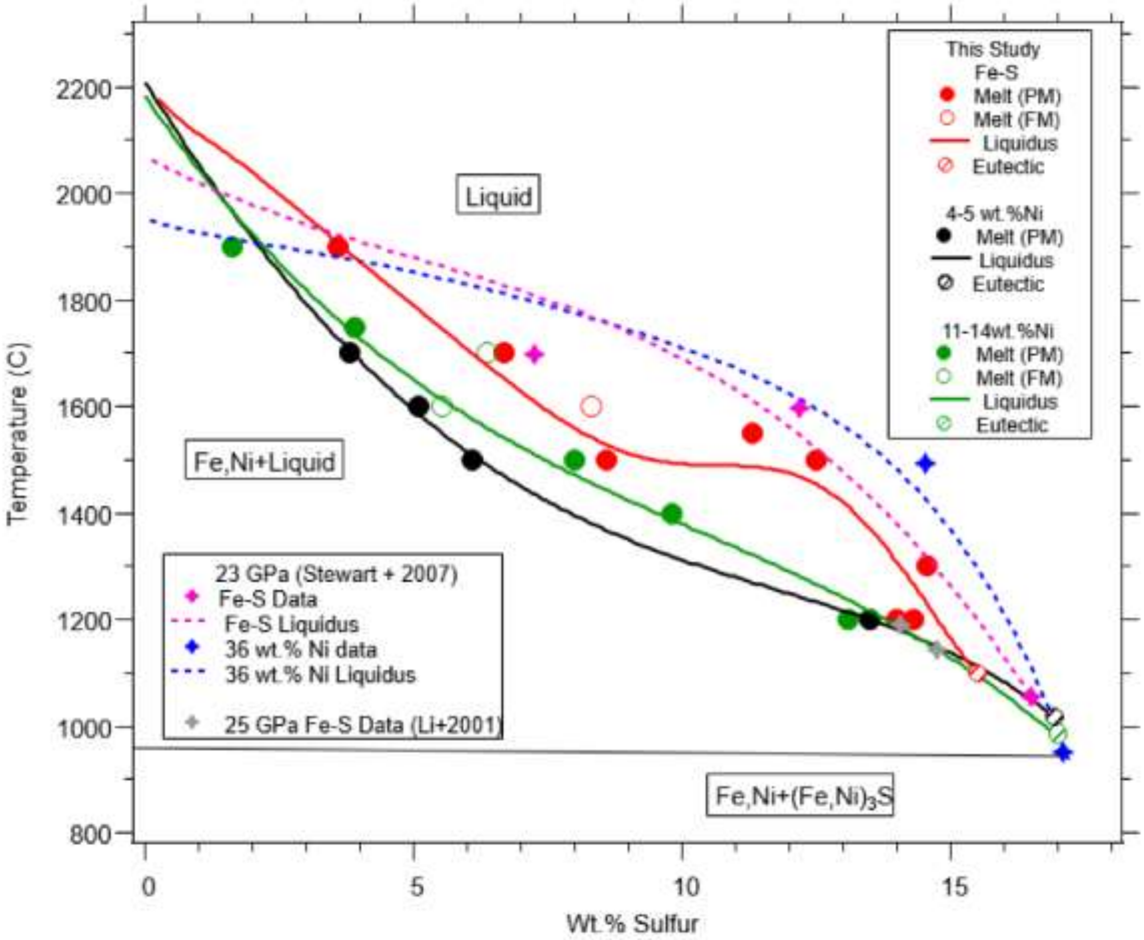

Figure 9: Comparison of results between this study and literature data near 24 GPa. For this study, the symbols are the same as in Figures 7 and 8. The eutectic points interpolated from Stewart et al. (2007), Zhang et al. (2008), and Li et al. (2001) are shown as green, black, and red hatched circles. The melting points of Fe and Fe-Ni are calculated from Anzellini et al. (2013) and Boccato et al. (2017). The dashed pink and blue lines are liquidus curves proposed by Stewart et al. (2007) for the Fe-S and (Fe, Ni)-S (36 wt.%Ni), respectively. The pink and blue stars are the experimental data from Stewart et al. (2007) for the Fe-S and (Fe, Ni)-S (36 wt.%Ni), respectively. The grey stars are experimental data from Li et al. (2001) at 25 GPa.

3.6.3 (Fe, Ni)-S liquidus curves at 5.1 GPa to 40 GPa

Four previous studies determined the liquidus curves of the (Fe, Ni)-S system at 5.1, 20, 23, and 40 GPa. Experiments at 5.1 and 20 GPa indicated that Ni lowers the Fe-S liquidus (Liu and Li, 2020; Gilfoy and Li, 2020), whereas those at 23 and 40 GPa observed little to no change when Ni was added to the Fe-S liquidus (Stewart et al., 2007). In this study, we found that the (Fe, Ni)-S liquidus for the 11-14 wt.% Ni and 4-5 wt.% Ni systems are at lower temperatures than that of the Fe-S system at 24 GPa. The discrepancy between this study and Stewart (2007), which focused on determining the eutectic melting points of the Fe-S and (Fe, Ni)-S system, and thus had only one or two data points on the liquidus, may be a result of different experimental goals.

The effect of the Ni is not yet well understood. Based on this study and Stewart et al. (2007), it appears that 4-5 wt.% Ni lowers the melting point of the Fe-S system more than 11-14 wt.% Ni, which, in turn, lowers the melting point of the Fe- S system more than 36 wt.% Ni (Figure 9). In other words, adding a small amount of Ni has a large effect in depressing the melting point, but increasing the amount of Ni shifts the liquidus curve towards the Ni-free system. To date, the (Fe, Ni)-S liquidus and eutectic have been investigated in systems with different concentrations of Ni, and therefore the results are not directly comparable (Stewart et al., 2007; Zhang and Fei, 2008; Morard et al., 2011; Mori et al., 2017; Liu and Li, 2019; Gilfoy and Li, 2020). Therefore, a range of Ni concentrations needs to be explored to constrain how different concentrations of Ni impact the Fe-S liquidus.

Section 4: Implications for Mercury’s Core

In this study, we observe that at 24 GPa, Ni depresses the Fe-S melting point by as much as 300°C (Figure 10). Qualitatively this is consistent with previous studies at < 7 GPa (Liu and Li, 2020) and an indirect comparison between two studies at 20 GPa (Pommier 18; Gilfoy and Li, 2020). The effect of Ni varies with pressure. At 5.1 GPa, Ni depresses the Fe-S liquidus the most at low sulfur concentrations and the least at 10 wt.% sulfur. The opposite is true at 20 GPa. At 24 GPa, the maximum effect occurs at the inflection point with ~11-13 wt.% S (Figure 10).

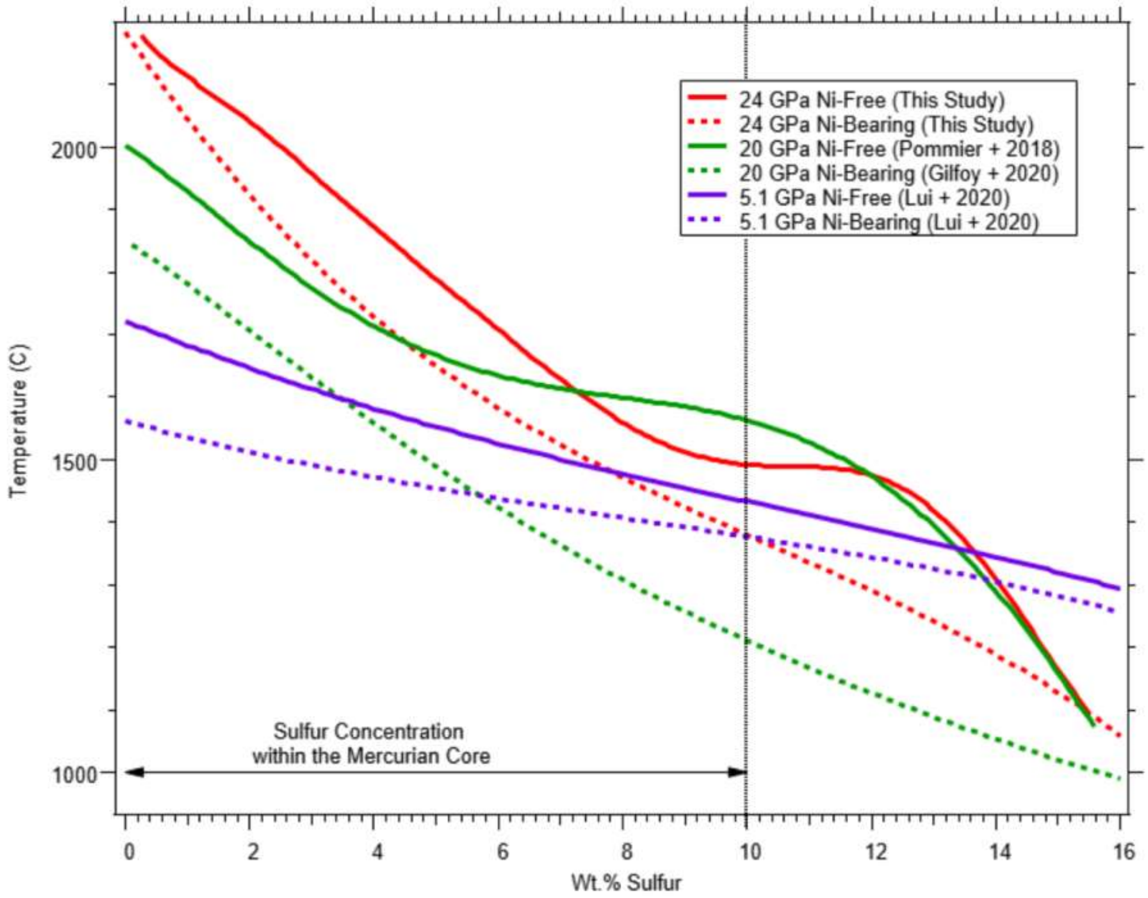

Figure 10: Fe-S and (Fe, Ni)-S system compared to literature. The Fe-S liquidi are solid curves, and the (Fe, Ni)-S liquidi are dashed curves. Red are results from this study, where the 11-14 wt.% liquidus is used. Green are the published liquidi at 20 GPa (Pommier et al., 2018; Gilfoy and Li, 2020). Purple are published liquidi at 5.1 GPa (Liu and Li, 2020).

For model compositions of the Mercurian core containing 0-10 wt.% sulfur, Ni changes the melting point of Fe-S by + 2˚C/ wt.% Ni at 0 wt.% S, and up to ~ -300 ˚C for 1-16 wt.%S (Figure 11). Figure 11, directly compares the pressure-temperature liquidi for the Fe-S and (Fe, Ni)-S system from 5.1 to 24 GPa. Ni-Free (Fe-S) liquidi are fifth-order polynomial fits to published data (Fei et al., 2001; Stewart et al., 2007; Chen et al., 2008; Buono and Walker, 2011; Pommier et al., 2018) and this study. Ni-Bearing (Fe-Ni-S) liquidi are linear fits between published data (Liu and Li, 2020; Gilfoy and Li, 2020) and this study. Stewart et al. (2007) is omitted from the fit in the Fe-S system at 23 GPa and is not included for the (Fe, Ni)-S system at 23 or 40 GPa due to the small sample size.

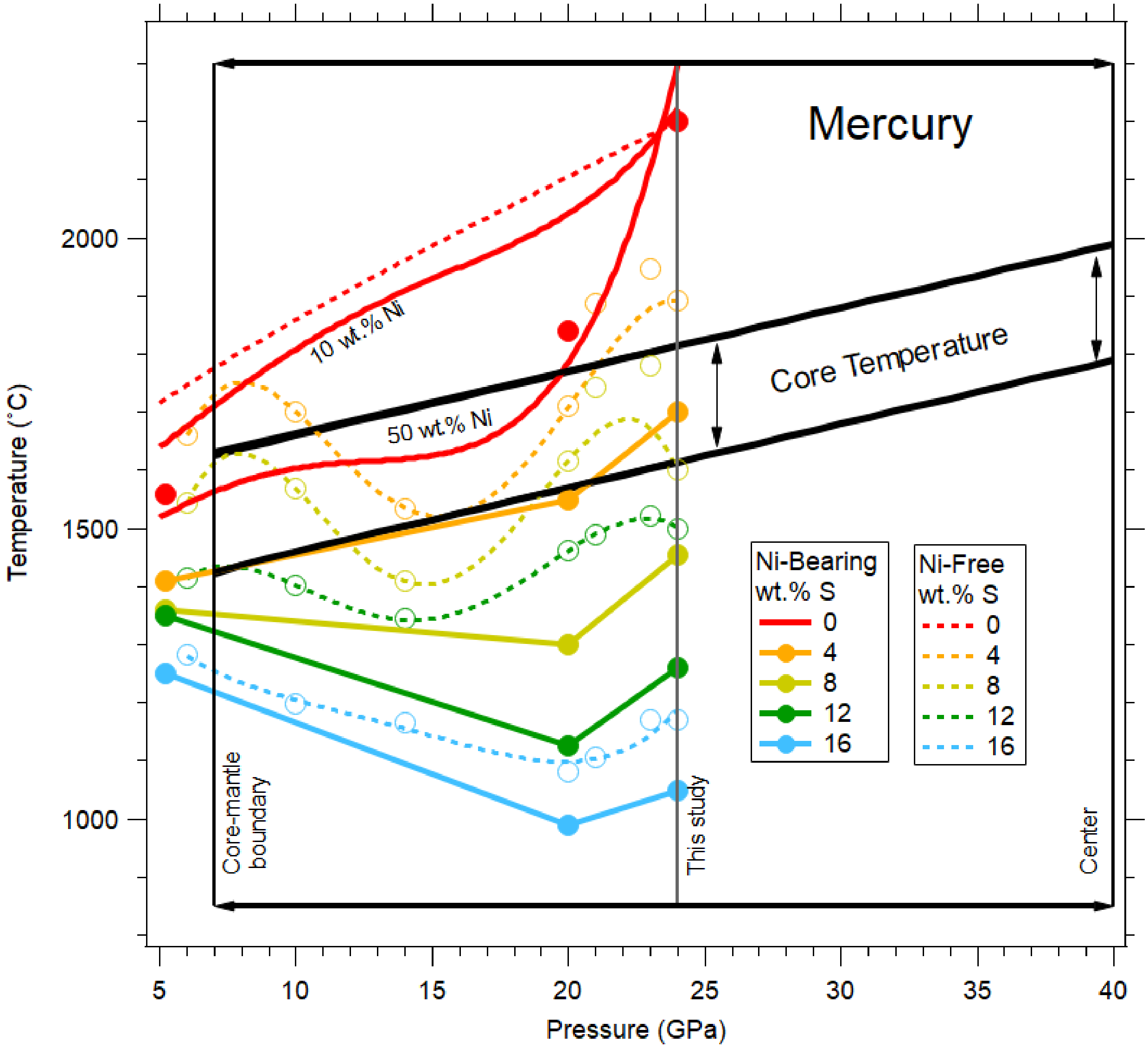

Figure 11: Pressure-temperature Fe-S phase diagram for the Mercurian core. The core temperature is proposed by Chen et al. (2008). Ni-Free (Fe-S) liquidi are fifth-order polynomial fits to published data (open circles) at variable sulfur concentrations. Ni-Bearing (Fe-Ni-S) liquidi are linear fits between published data (closed circles) at variable sulfur concentrations. The nickel concentration ranges from 50 wt.%, 9 wt.%, to 11-14 wt.% at 5.1, 20, and 24 GPa, respectively (Liu et al., 2020; Gilfoy et al., 2020). The melting point of Fe-Ni is reported at 10 and 50 wt.% Ni, calculated on the basis of 2 to -7°C/wt.%Ni at high to low pressure, respectively (Boccato et al., 2017; Liu et al., 2020; Gilfoy et al., 2020).

According to current estimates, the temperature profile of the Mercurian core follows an adiabatic gradient of 11 K/GPa, with a base temperature of 1427-1627 °C (1700 - 1900 K) at its core-mantle boundary (Christensen, 2006; Chen et al., 2008). With these thermal models and considering effects of Ni on the melting points, the core could be solid if it contains no sulfur, it would be partially molten at < 4 wt.% S, and it would be fully molten at > 4wt.% S. This conclusion allows for a broad range of possible core compositions for Mercury (details in appendix).

A sulfur concentration of 0-10 wt.% can be directly compared to the Mercurian core. Given the current conditions proposed for the Mercurian core (CMB temperature 1427 and 1627 ° C, 7-40 GPa, partially molten) and the effect Ni has on Fe-S system, < 4wt.% S would be the only composition that is partially molten with a solid inner core. Previous studies predict the core is partially molten via the precipitation of Fe-snow or the formation of a Fe-S shell at the core-mantle boundary (Chen et al., 2008; Malavergne et al., 2010). If we assume the same solidification models for the addition of Ni, the core-mantle boundary would be at a lower temperature than the Fe-S system. We infer the core-mantle boundary would be 100-200° C lower than the published condition for the CMB (Figure 11). Therefore a core-mantle boundary temperature of 1227-1627 °C would result in a partially molten core for the (Fe, Ni)-S system. Given the change in core-mantle boundary temperature and the variation of Ni's depression of the Fe-S liquidus, the adiabat may not be 11K/GPa. Instead, a new adiabat may need to be constructed to encompass the (Fe, Ni)-S system.

Section 5: Conclusions

Experiments on the Fe-S binary system at 14 GPa confirmed the presence of an inflection point at ~10 wt.% sulfur on the Fe-rich side of the eutectic point. Furthermore, a new constraint on the liquidus curve on the S-rich side of the eutectic point suggests that the existing model needs to be significantly revised towards lower temperatures. Experimental data at 24 GPa show that on the iron-rich side of the eutectic point, the Fe-S liquidus curve has an inflection point at ~ 11.5 wt.%

sulfur, whereas the (Fe, Ni)-S liquidus curve is smooth. The presence of Ni lowers the melting point of the Fe-S system by as much as 300 ˚C. The effect of Ni appears to have a complex dependence on pressure and composition. Further studies are needed to quantify the effect and explore the implications for the thermal and chemical state of Mercury's core and the origin of its weak magnetic field.

Section 6: Appendix

6.1 Figures

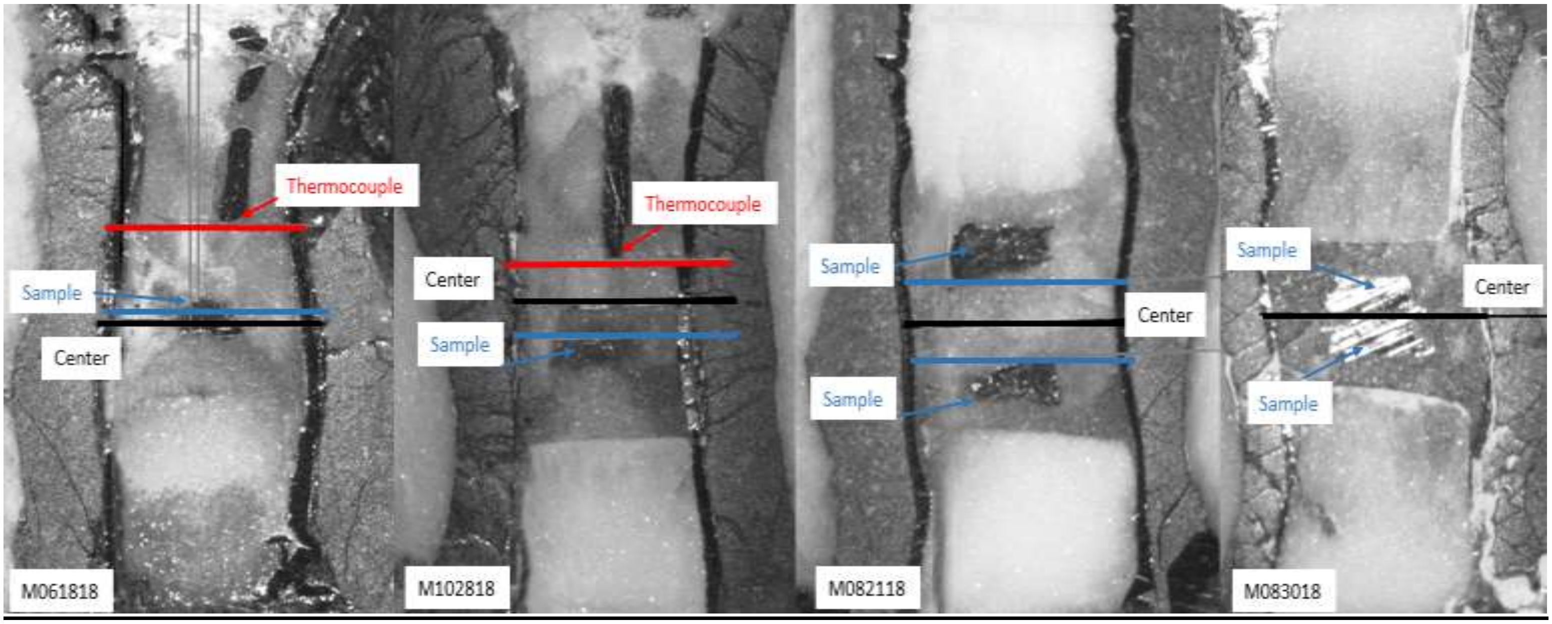

Figure A1: Experimental configuration from sample M061818, M102818, M082118, and M083018. M061818 and M102818 are single chamber experiments. M102818 is the ideal experimental configuration using 1.5 Al_2O_3 plug, while M061818 is an acceptable experimental configuration using a 2.1 Al_2O_3 plug. M0821118 and M083018 are dual-chamber experiments. M083018 is the ideal experimental configuration that does not have a 0.25 mm Al_2O_3 sliver, while M082118 is an acceptable experimental configuration that does have a 0.25 Al_2O_3 sliver.

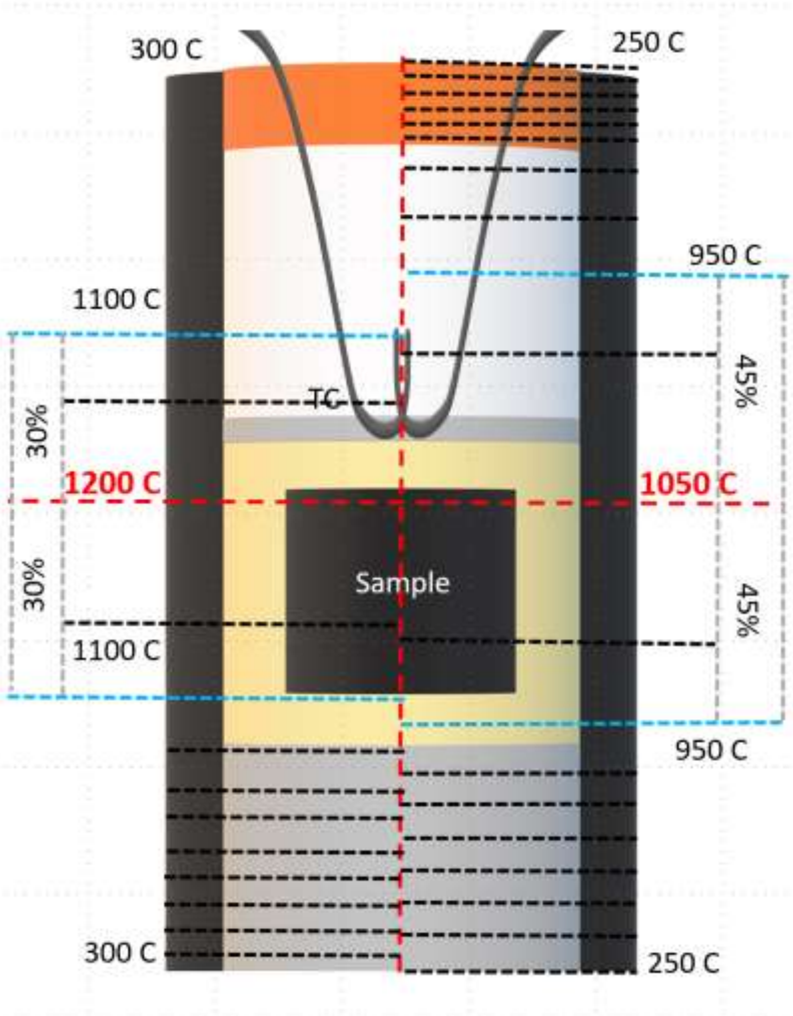

Figure A2: Schematic temperature distribution of the 8/3 assembly. The center is marked with the dashed red line, while the 100° temperature boundaries are marked in blue. The left side of the chamber has a max temperature of 1200°C and has a 100° drop of 30% from the center (Hernlund et al., 2006). The right side of the chamber has a max temperature of 1050°C and has a 100° drop of 45% from the center (Leinenweber et al., 2012) as the max internal temperature increases the temperature gradients within the cell increase.

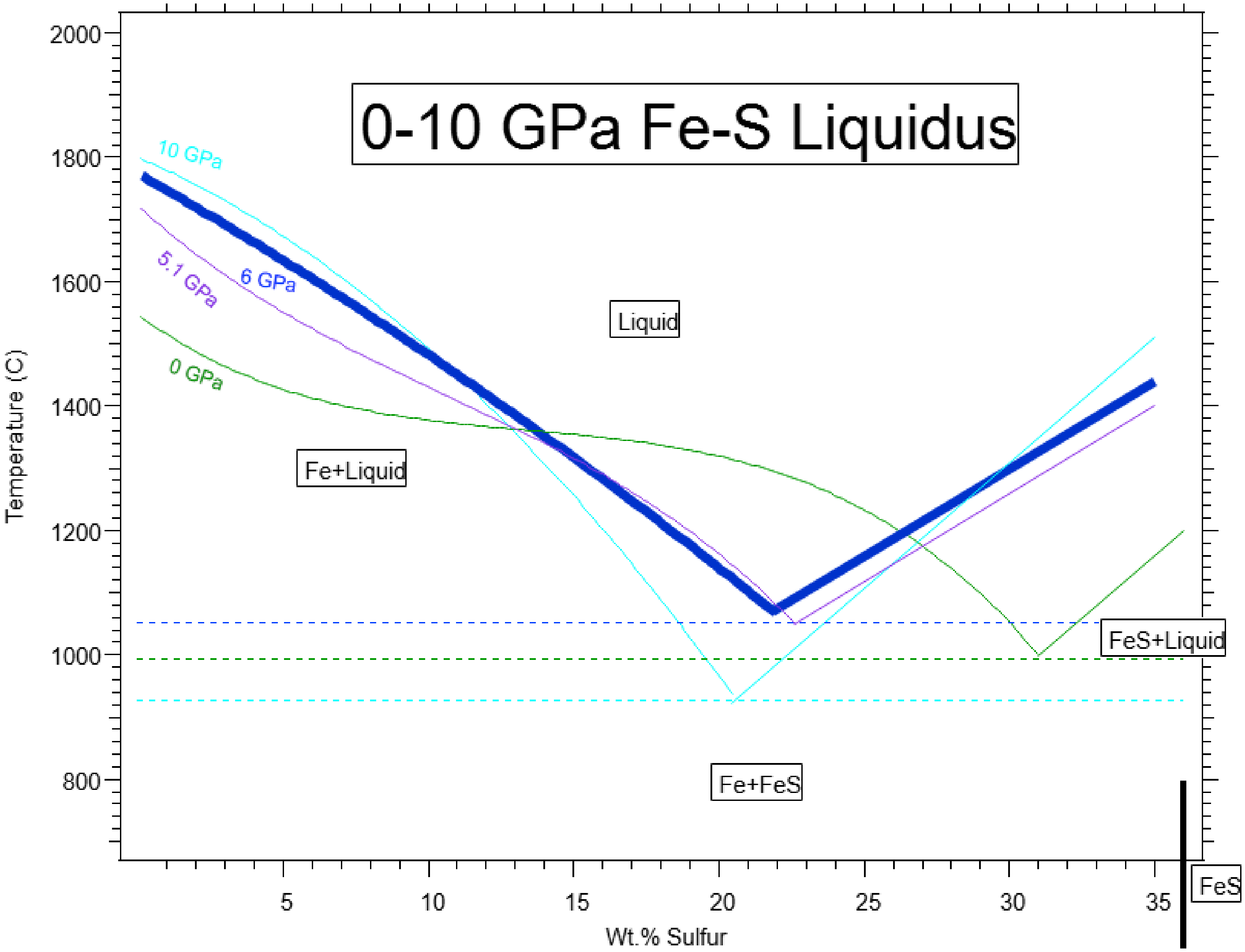
0-10 GPa Fe-S Liquidus
10 GPa
6 GPa
5.1 GPa
0 GPa
Liquid
Fe+Liquid
FeS+Liquid
Fe+FeS
FeS
Temperature (C)
2000
1800
1600
1400
1200
1000
800
Wt.% Sulfur
5
10
15
20
25
30
35

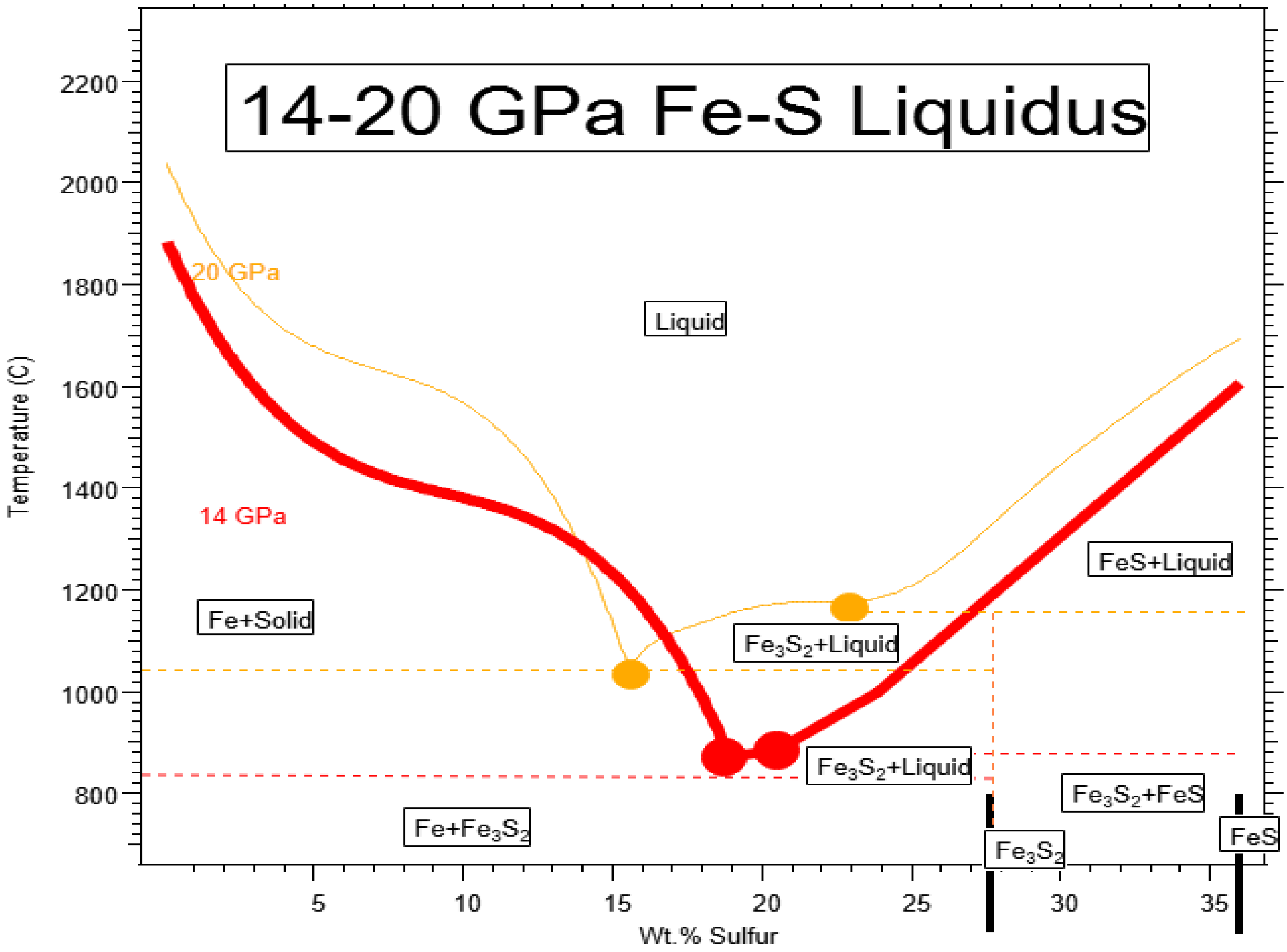
14-20 GPa Fe-S Liquidus
20 GPa
14 GPa
Liquid
Fe+Solid
Fe_3S_2+Liquid
Fe_3S_2+Liquid
FeS+Liquid
Fe_3S_2+FeS
Fe+Fe_3S_2
Fe_3S_2
FeS
Temperature (C)
2200
2000
1800
1600
1400
1200
1000
800
5
10
15
20
25
30
35
Wt.% Sulfur

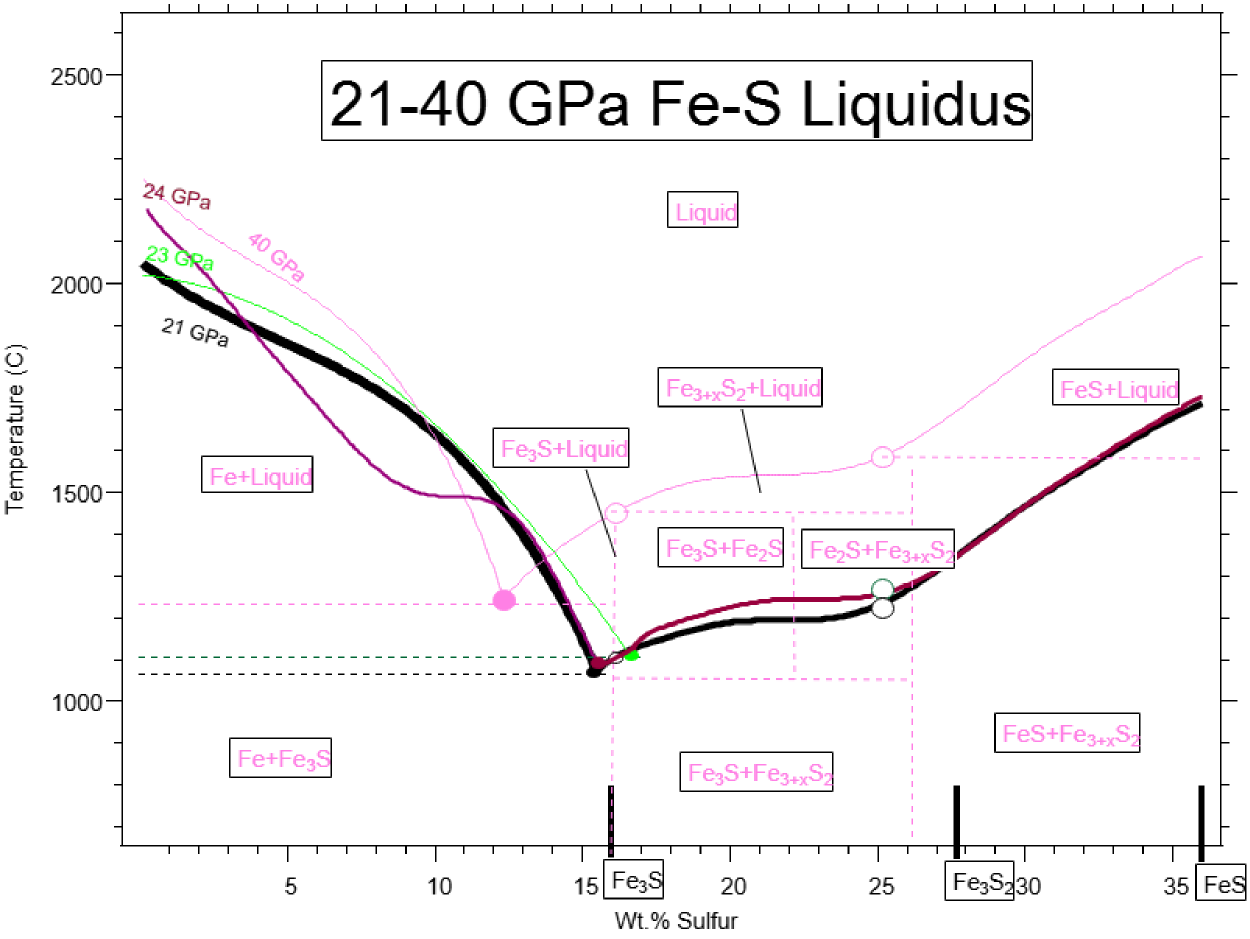
21-40 GPa Fe-S Liquidus
24 GPa
40 GPa
23 GPa
21 GPa
Liquid
Fe+Liquid
Fe$_3$S+Liquid
Fe$_{3+x}$S$_2$+Liquid
FeS+Liquid
Fe$_3$S+Fe$_2$S
Fe$_2$S+Fe$_{3+x}$S$_2$
Fe+Fe$_3$S
Fe$_3$S+Fe$_{3+x}$S$_2$
FeS+Fe$_{3+x}$S$_2$
Fe$_3$S
Fe$_3$S$_2$
FeS
2500
2000
1500
1000
Temperature (C)
5
10
15
20
25
30
35
Wt.% Sulfur

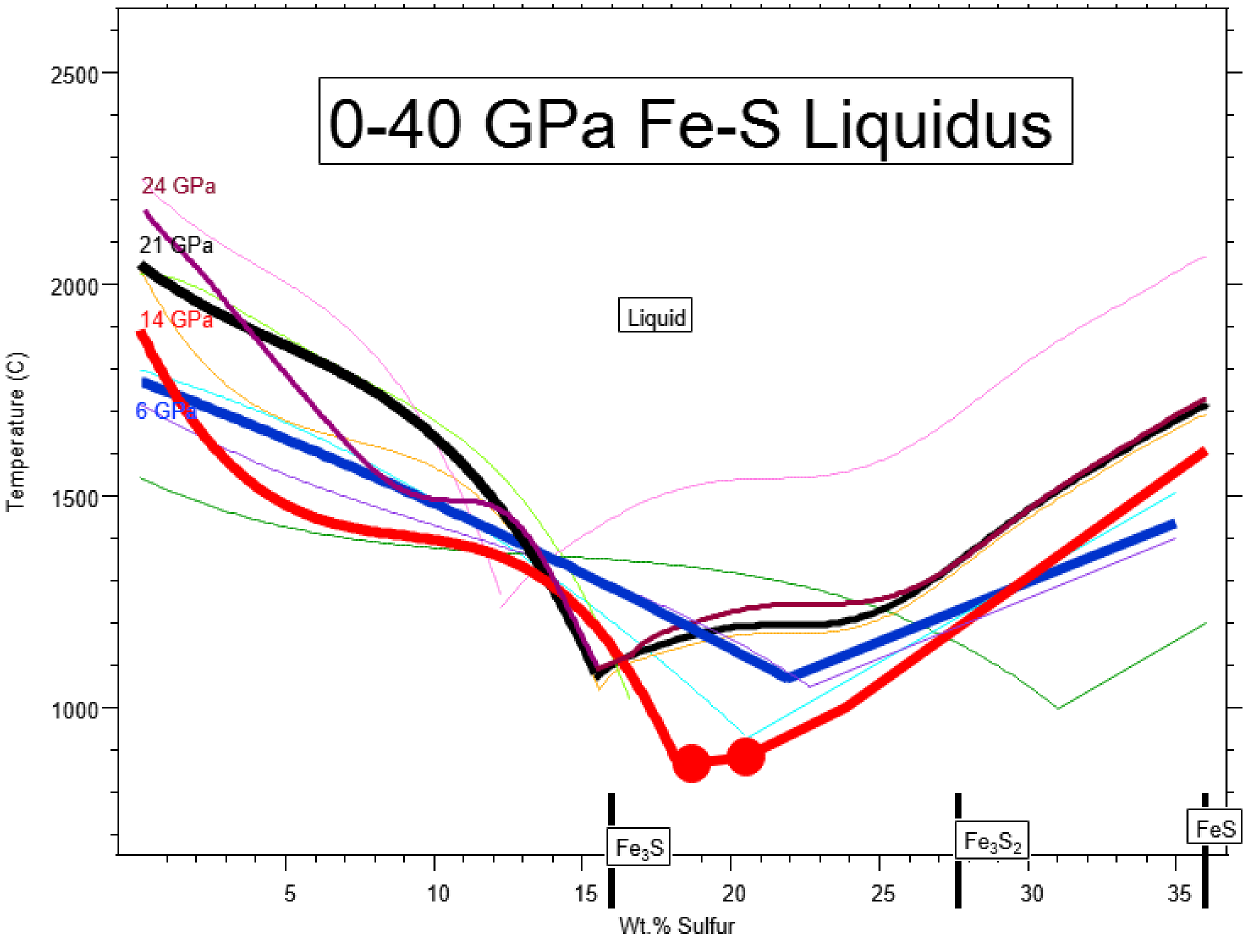

Figure A3: Fe-S liquidus 1 bar-40 GPa. The liquidus is based on published and experimental data. Between 1 bar-10 GPa, Fe and FeS are formed at the eutectic. 0 GPa (dark green) is based on Friedrich (1910) and Miyazaki (1928). 5.1 GPa (purple) is based on Liu and Li, 2020 . 6 GPa (dark blue) is based on Buono et al., 2013. 10 GPa (cyan) is based on Chen et al., 2008. Between 14-21 GPa Fe_3S_2 and Fe is formed at the eutectic. 14 GPa (red) is based on this study, and Chen et al., 2008. 20 GPa (yellow) is based on Pommier et al., 2018. Between 21-40 GPa Fe_3S and Fe is formed at the eutectic. 21 GPa (black) is based on Fei et al., 2000. 23 GPa (light green) is based on Stewart et al., 2007. 24 GPa (maroon) is from this study. 40 GPa (pink) is based on Stewart et al., 2007. On the sulfur-poor side of the eutectic, the 1 Bar, 14 GPa, and 20 GPa liquidii are non-ideal and experience and an inflection point. While the sulfur-rich side is an extrapolation based on the melting point of FeS and published eutectic constraints.

6.2 Tables

Experiment Name	Thermocouple Distance from the center as a %	Sample distance from the center as a %	Temperature (C)	Max Distance	Thermocouple Unc	Sample Unc	Systematic Unc	Total Unc
Ni-free								
M062718	<23.4	0.7	1900	21	111	3	111	114
M061118	32.1	-17.6	1800	22	143	-78	164	166
M083018*	9	0	1700	24	38	0	38	45
M061318	18.3	11.2	1650	24	75	46	88	92
M071318*	9	24	1600	25	36	96	102	105
M060818	<22.9	0	1500	26	87	0	87	90
M062018	<16.2	5.4	1550	26	63	21	66	71
M082818*	9	0	1500	26	34	0	34	42
M062518	14.8	5	1300	29	51	17	54	59
M061818	<29.8	0	1200	30	98	0	98	101
M082118*	9	9.4	1200	30	30	31	43	50
Ni-bearing								
M111518	18.1	12.8	1900	21	86	61	105	108
M111618	5.3	11.2	1750	23	23	49	54	59
M083018*	9	0	1700	24	37	0	38	45
M102818	<14.7	10.2	1700	24	62	43	75	80
M111418	12.2	9.4	1600	25	49	38	62	66
M071318*	9	24	1600	25	36	96	102	105
M102618	<29.1	9.9	1500	26	110	38	116	119
M082818*	9	8.8	1500	26	34	33	48	54
M110718	3.9	12.5	1400	28	14	45	47	53
M102518	7.8	14.9	1300	29	27	51	58	63
M110818	15.6	14.8	1200	30	51	49	71	75
M082118*	9	16.5	1200	30	30	54	62	67

Table A1: The distance ratio is determined by subtracting the center value by the location of the thermocouple/sample, then dividing the value by the center measurement. The thermocouple is placed above the centerline, and the sample is below the centerline. In rare cases it may be on the opposite side. These cases are denoted with a negative sign. Cases marked with a * mean they were dual-chamber experiments. Therefore, the thermocouple distance ratio is the value observed from the calibration experiment M062318. When the distance is highlighted in red, it indicates the value is outside of the % ranges consistent with 100° uncertainty. The < symbol indicated the thermocouple is only partially observed, and the distance may be smaller than the recorded value.

		Temperature (C)					
Reference	Pressure GPa	0 wt.% S	4 wt.% S	8 wt.% S	12 wt.% S	16 wt.% S	20 wt.% S
Figure A6, Ni-Free							
Buono and Walker 2011	6	1710*	1660	1540	1410	1280	1140
Chen et al., 2008	10	1860*	1700	1570	1400	1210	960
Chen et al., 2008	14	1960*	1540	1410	1340	1170	880#
Pommier., 2018	20	2110*	1710	1620	1460	1080	1170#
Fei et al., 2001	21	2110*	1890	1770	1550	1110	1190#
Stewart et al., 2007	23	2180*	1910	1780	1520	1100	1230#
This Study	24	2200*	1870	1560	1480	1100	1230#
Stewart et al., 2007	40	2540*	2040	1820	1310	1450#	1530#
Figure A8, Ni-Bearing							
Reference	Pressure GPa	0 wt.% S	4 wt.% S	8 wt.% S	10 wt.% S	12 wt.% S	16 wt.% S
Liu and Li., 2020	5.2	Range of values. Published A4 and A6. Anzellini et al. (2013) modified Figure 11.	1410	1360	1380	1350	1250
Gilfoy and Li, 2020	20		1550	1300	1200	1125	990
This Study	24		1700	1455	1370	1260	1050
Stewart et al., 2007	40		1990	1800	1650	1450	1240

Table A2: Published data for Figures 11, A4 and A6. Each data point was approximated by digitizing the liquidus curve of the corresponding study; this attributes a 30° uncertainty to each point. 20 wt.% was extrapolated for the Fe-S system but no the (Fe, Ni)-S system.
*represents the melting point of iron calculated by Anzellini et al. (2013).
represents extrapolated liquidii on the S-rich side of the eutectic.

6.3 Uncertainties in (Fe, Ni)-S Solidification Models

Nickel is predicted to lower the CMB temperature by 100-200°C; this decrease in temperature has the potential for the observation for new solidification regimes for the Mercurian core. However, literature for the (Fe, Ni)-S system is limited and full of uncertainties. There are four primary (Fe, Ni)-S liquidus studies 5.1, 20, 23, and 40 GPa (Stewart et al., 2007; Pommier et al., 2018; Liu and Li, 2019; Gilfoy and Li, 2020). 5.1 GPa contains 50 wt.% Ni, 20 GPa contained 9 wt.% Ni, 23, and 40 GPa contains 36 wt.% Ni. From this study, we observe that 4-5 and 11-14 wt.% Ni lowered the Fe-S liquidus at 24 GPa and 36 wt.% Ni increased/had no effect on the Fe-S liquidus at 23 GPa (Figure 9). The concentration of Ni affects the Fe-S liquidus differently;

therefore, studies implementing solidification regimes for the (Fe, Ni)-S liquidus must have similar concentrations of Ni.

Studies at 20 and 24 GPa are comparable because they have similar Ni concentrations; however, studies at 5.1, 23, and 40 GPa are not comparable because they have higher Ni concentration. In section 4, we implement 5.1 GPa to constrain the Fe-Ni-S liquidi; this introduces uncertainty in the CMB temperature. We infer a lower Ni concentration would result in a larger depression of the (Fe, Ni)-S system (similar to observations at 23 and 24 GPa). However, since the literature is sparse, we implemented the 5.1 GPa constraint regardless of the Ni concentration.

Solidification models have uncertainties in Ni concentration, the thermal profile of the core, and experimental uncertainties. The experimental uncertainties impose a 50-150 degrees uncertainty on each curve, implying the exact location of solidification is unknown. Given the number of uncertainties associated with solidification models, Fe-S and (Fe, Ni)-S solidification predictions can be found in section 6.4.

6.4 Solidification Regime Implications

We calculate a pressure-temperature phase diagram of the Fe-S and (Fe, Ni)-S system to infer potential solidification regimes of the Mercurian core (Figures A4 and A6). Published data are solid, and open circles in Figure A4 and A6 are detailed in Table A2 (Appendix). For the Fe-S system, the published data was fit with a fifth-order polynomial. Low weight percent S liquidi exclude data at 21 and 23 GPa. The data points are excluded because the liquidus shape is not well defined and contradicts the results found in this study. The liquidi are extrapolated linearly between 24 and 40 GPa because there is no published data within that region. For the (Fe, Ni)-S system, the published data was fit linearly between individual points.

Various solidification regimes were inferred based on the intersection of the Mercurian adiabat with the Fe-S and (Fe, Ni)-S liquidus. We apply two different adiabats A1 and A2; the adiabats have a slope of 11 K/GPa. A1 and A2 represent a core-mantle boundary temperature of 1427 and 1627 ° C (1700 and 1900 K), respectively (Chen et al., 2008). The slope of 11 K/GPa was calculated by Chen et al. (2008) using material properties from Turcotte and Schubert. (2002) Christensen (2006), and Boehler (1992).

6.4.1 Fe-S Core

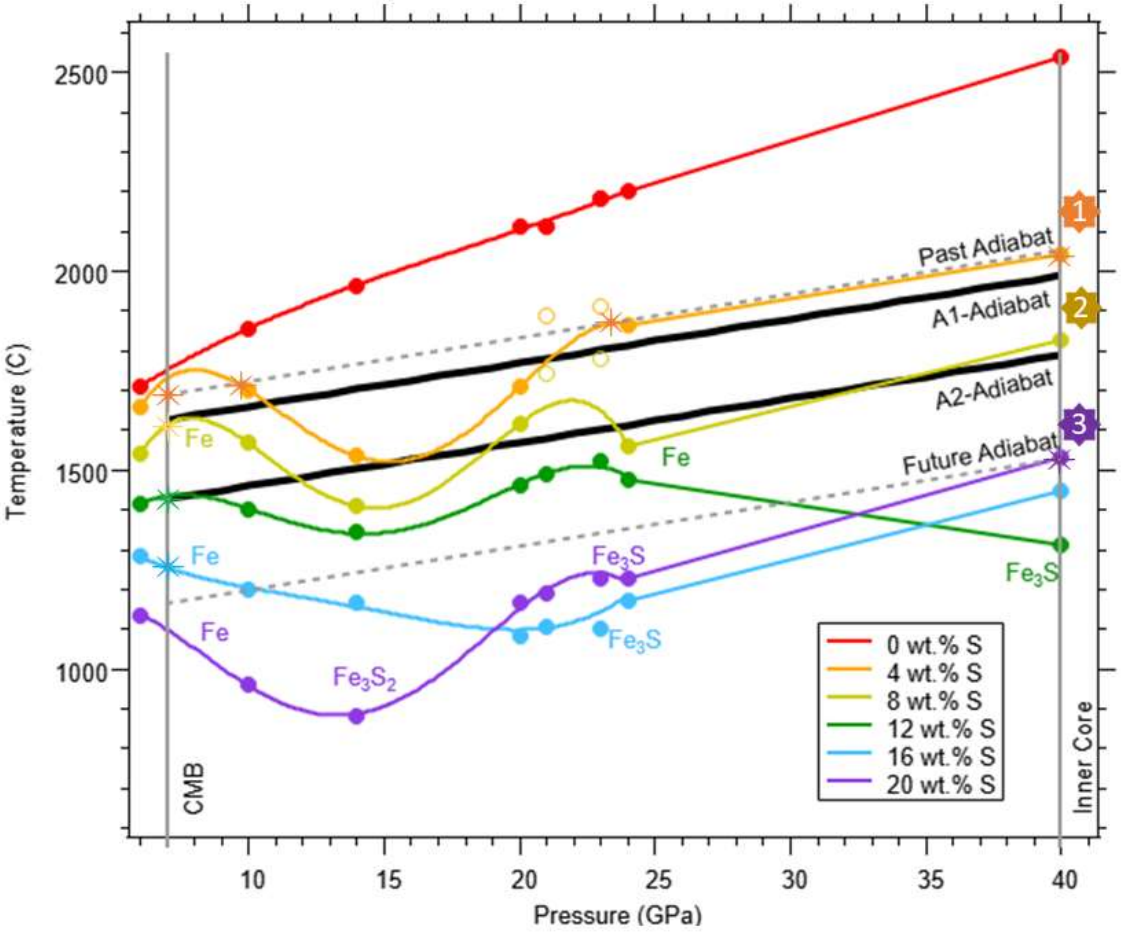

Figure A4: Pressure-temperature Fe-S phase diagram with Mercurian adiabats. Adiabats A1 and A2 are from Chen et al. (2008) and represent the estimated temperature range for the core. Past and future adiabats are projects to show intersection with the liquidii for the Fe-S core with various sulfur contents, as determined by liquidus data from this study and literature (closed circles). As the core of Mercury cools, the adiabat shifts to lower temperature and intersects the Fe-S liquidus. If iron or Fe_3S precipitates, the sulfur content of the core would increase. Locations of intersection are labeled on the figure as * and the solidification regime number is to the right of the figure.

We propose three different solidification regimes for the core of Mercury. The first regime (<8 wt.% S) iron precipitates at 7, 10, 23, and 40 GPa, then as the composition becomes more sulfur-rich iron precipitates at 7 GPa, as the composition continues to shift iron precipitates at 7 GPa and Fe_3S precipitates at 38-40 GPa. The second solidification regime (8-16 wt.% S) iron precipitates at 7 GPa, then Fe_3S at 38-40 GPa. The third regime (>16 wt.% S) Fe_3S precipitates at 38-40 GPa. Each solidification regime is shown in Figure A5.

Iron precipitating in the form of iron snow has been proposed to occur within numerous small terrestrial bodies. However, due to the drastic change in liquidus shape, we observe numerous locations of snow precipitating within the core of Mercury. The interactions between Fe and Fe_3S_2 at 10-14 GPa results in a liquidus drop by 100-300°C. For Mercury, this scenario results in iron precipitation at < 14 GPa, where FeS is stable. The interactions between Fe and Fe_3S at 23 GPa results in a 100-300°C decrease between 23 and 24 GPa. This scenario results in iron precipitation at 23 GPa.

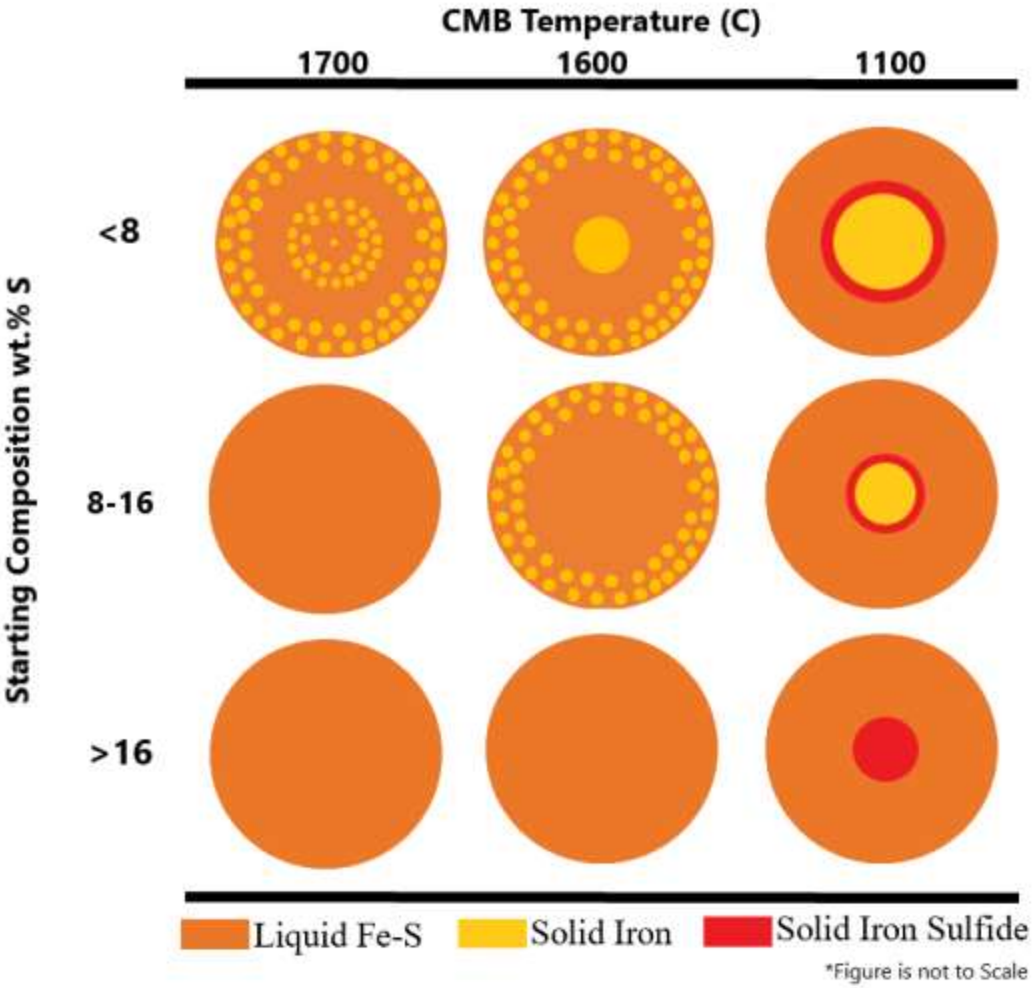

Figure A5: Proposed solidification regimes for the Mercurian core for a range of sulfur concentrations through time. Orange represents a molten iron-sulfur alloy, yellow represents a pure iron, and red represents iron sulfide (Fe_3S). The top row represents an initial core composition with <8 wt.% S. As Mercury cools iron precipitates at 7, 10, 23, and 40 GPa, then as the bulk molten core composition becomes more sulfur-rich iron precipitates at the core-mantle boundary. As the Fe-S melt increases in sulfur content, an iron sulfide forms at the center of the planet. The second row represents an initial composition with 8-16 wt.% S. As Mercury cools iron precipitates at the core-mantle boundary, and the composition shifts producing an iron sulfide at the center of the planet. The third row represents an initial composition with >16 wt.% S as Mercury cools an iron sulfide forms at the center of the planet.

The Fe-S system is detailed in the literature and has eight liquidus studies in the pressure range consistent with Mercury. The limited data set introduces limitations and extrapolations in the Fe-S system pressure-temperature phase diagram. The limitations are accounted for at high pressure using linear interpolation. The lower pressure conditions introduce artifacts in the liquidus fit; these artifacts are ignored in the solidification regime predictions.

6.4.2 (Fe, Ni)-S Core

Unlike the Fe-S system, the (Fe, Ni)-S system is sparsely detailed in the literature. There are four central studies at 5.1, 20, 23, and 40 GPa, but due to the large discrepancy between this study and 23 GPa, small data set, increased Ni concentration, the 23 GPa liquidus is omitted. There are significant uncertainties associated with 5.1 and 40 GPa, due to a large concentration of Ni added to each study. These studies are included to provide constraints. The published data are shown in Figure A6; a pressure-temperature phase diagram and the Fe-Ni-S liquidi are linear interpolations between published data points. The adiabats are projected into the future to detail intersections with the proposed liquidi.

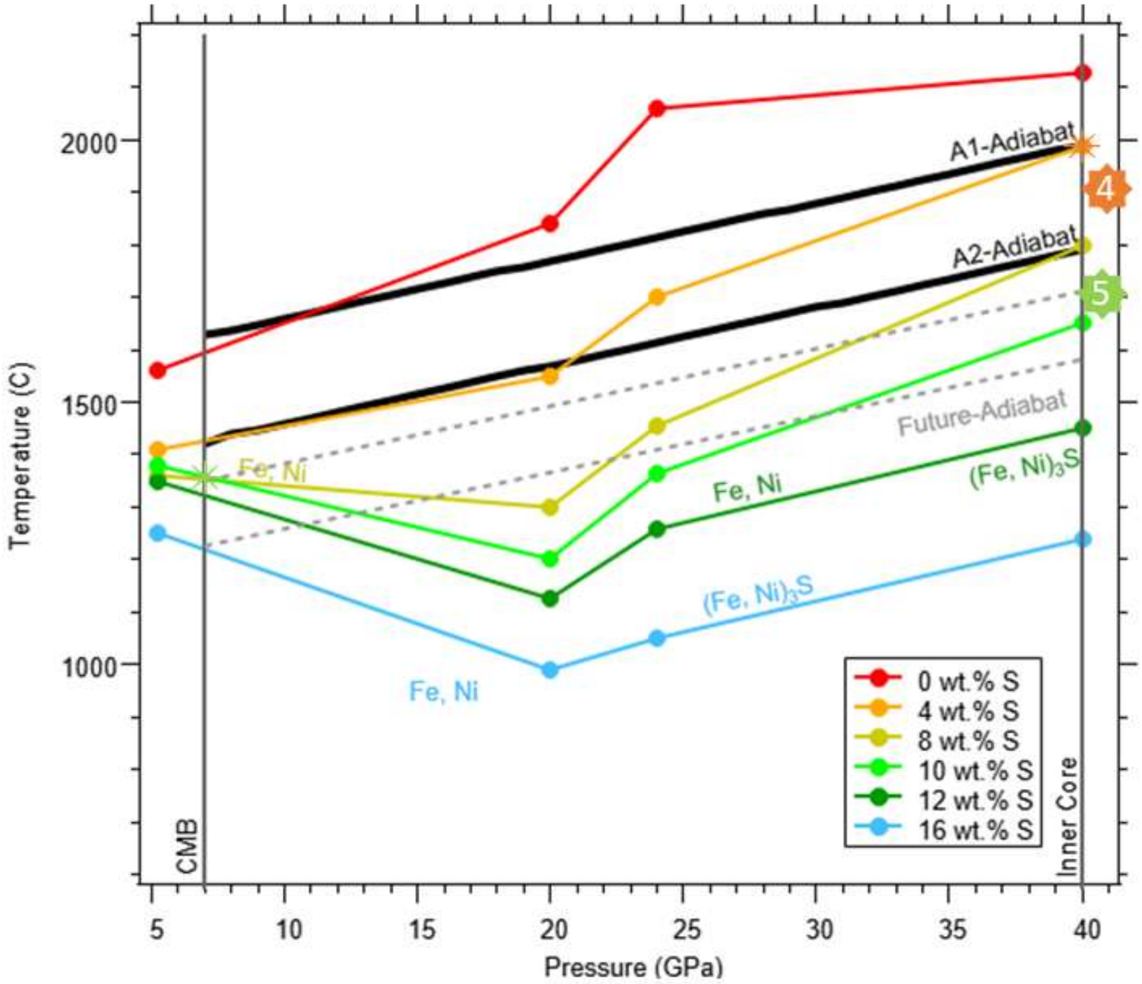

Figure A6: Pressure-temperature (Fe, Ni)-S phase diagram with Mercurian adiabats. Adiabats A1 and A2 are from Chen et al. (2008) and represent the estimated temperature range for the core. Past and future adiabats are projects to show intersection with the liquidii for (Fe, Ni)-S core with various sulfur contents, as determined by liquidus data from this study and literature (closed circles). As the core of Mercury cools, the adiabat shifts to lower temperature and intersects the Fe-S liquidus. If iron precipitates, the sulfur content of the core would increase. Locations of intersection are labeled on the figure as * and the solidification regime number is to the right of the figure. Constraints at 5.1 and 40 GPa have different Ni concentrations.

Each of the published (Fe, Ni)-S liquidi are proposed to be ideal, resulting in a gradual increase in melting point with pressure. The eutectic shift between 5.1 and 20 GPa results in a lower melting point at 20 GPa than at 5.1 GPa for high-sulfur concentrations. This gradual decrease in temperature results in different solidification regimes; these regimes are predicted based on the intersection of the Mercurian adiabat with the (Fe, Ni)-S liquidus. 20 wt.% S is not considered for the (Fe, Ni)-S system because there are no published studies are on the s-rich side of the eutectic with a similar Ni concentration.

We propose two new solidification regimes for the core of Mercury, labeled 4 and 5. The fourth regime occurs when the bulk composition is <8 wt.% sulfur; Fe-Ni solidifies at 40 GPa as the sulfur concentration increases Fe-Ni solidifies at the core-mantle boundary (7 GPa). The fifth solidification regime occurs when the bulk composition is 10-12 wt.% sulfur; Fe-Ni solidifies at 7 GPa. Each solidification regime is detailed in Figure A6.

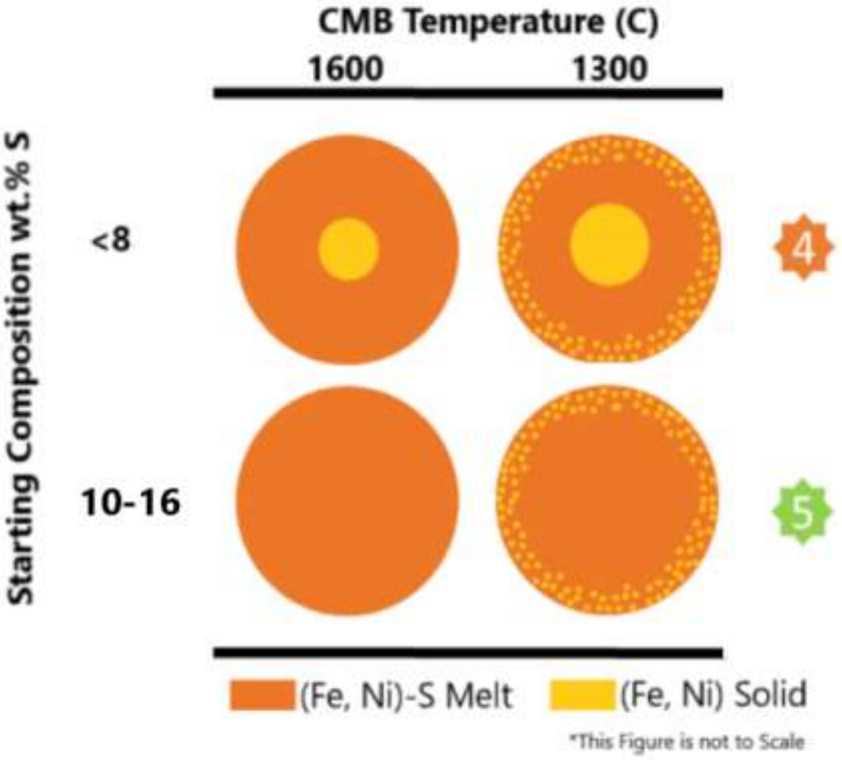

Figure A6: Proposed solidification regimes for the Mercurian core for a range of sulfur concentrations through time. Orange represents a molten iron-nickel-sulfur alloy, and yellow represents a pure iron-nickel. The top row (regime 4) represents an initial core composition with <8 wt.% S. As Mercury cools iron-nickel forms at the inner core, then as the bulk molten core composition becomes sulfur-rich, iron-nickel precipitates at the core-mantle boundary, The second row represents an initial composition with 10-16wt.% S. Iron-nickel precipitates at the core-mantle boundary.

6.5 Implications for the Origin and future of Mercury's Magnetic Field

We have proposed five different solidification regimes for the core of Mercury. The most applicable regime is dependent on the presence of Ni. For the Fe-S system, regime 1 is the most applicable condition for the Mercurian core solidification (<8 wt.% S). For the (Fe, Ni)-S system, regime 4 is the most appropriate form of solidification (<8 wt.% S). To understand the most applicable solidifications regime is it essential to consider the location of the A1 an A2 adiabat.

For the Fe-S system, the A1 adiabat is located between 4-8 wt.% S; while, the A2 adiabat is located between 8-12 wt.% S. Given the bulk sulfur content of the core is 0-10 wt.% S the adiabat location is consistent with observations that the core must be partially molten (Margot et al., 2007). The adiabat location also reinforces the notion that light elements are within the Mercurian core because if the core were pure iron, then the core would be fully-solid.

Based on the experimental results, we can infer that Mercury began solidification via iron snow (precipitation) at 7 and 23 GPa. As the planet cooled, the adiabats decreased to the A1 and A2 adiabat detailed in Figure A5. Indicating that the sulfur content in the melt is currently between 4-12 wt.% sulfur, and the planet is actively precipitating iron snow at 7 GPa and possibly 10-23 GPa. The effect of iron snow may weaken a planetary magnetic field by slowing convection. In the case of this study, when iron-snow occurs in multiple locations, it weakens the dynamo more than iron snow occurring in one location. The occurrence of iron snow at 7, 10, and 23 GPa could explain why Mercury has been observed by Mariner 10 and MESSENGER as having a weak magnetic field (Ness et al., 1974, 1975, 1976). As Mercury transitions to iron-snow occurring solely at 7 GPa, it is possible, the intensity of the magnetic field could increase.

For the (Fe, Ni)-S system, the A1 adiabat is located between 0-4 wt,% S while the A2 adiabat is located between 4-8 wt.% sulfur. Given that the bulk sulfur content of the core is 0-10 wt.% S the adiabat location is consistent with observations from Margot et al. (2007). The adiabat location also reinforces the notion that light elements are within the Mercurian core. Since Mercury is predicted to have a magnetic field insulated by iron snow, the liquidii impose constraints on the current sulfur range and adiabat location. We infer the most applicable current liquid sulfur range is between 8-12 wt.%

The most applicable solidification regime is the formation of iron-nickel precipitation at the core-mantle boundary and 40 GPa (regime 4 or 5). The formation of iron-nickel snow can explain the decrease in magnetic field strength. However, it does not occur until the core-mantle boundary is about 1300 °C. This temperature is outside the predicted core-mantle boundary temperature range of 1427 - 1627 ° C (Boehler, 1992; Chen et al., 2008; Hauck II et al., 2013). The lower boundary of 1427 ° C, was based on experimental constraints on the solidification of Fe-S for the Si-shell model (Boehler, 1992; Malavergne et al., 2010a; Hauck II et al., 2013). We propose that Ni lowers the melting point of the Fe-S liquidus to 1227 ° C.

The lower adiabat directly impacts the proposed solidification regimes in this study. Given a lower adiabat, we predict the core of Mercury resembles the fourth solidification regime. We predict the initial bulk sulfur concentration was <8 wt.% S. This formed a partially molten core observed by Margot et al. (2007). Then as the core-mantle boundary cooled to 1300° C, iron-nickel snow precipitated from the core-mantle boundary, ensuring the magnetic field strength is weaker, as observed in Mariner 10 and MESSENGER.

The lower adiabat indirectly impacts the proposed solidification regime in published studies. The formation of an Fe-S shell surrounding an Fe-Si-S molten core is the widely accepted model for the Mercurian core (Malavergne et al., 2010). This study neglects the impact of Ni. Therefore, we infer an immiscibility gap persists between Fe-Ni-S and Fe-Ni-Si-S. In order for an Fe-Ni-S shell to surround an Fe-Ni-Si-S molten core, the adiabat must be at a condition consistent with solid Fe-Ni-S forming at 7-14 GPa. This condition occurs when the composition is >10 wt.% S and the core-mantle boundary temperature is <1300° C.

References

Anderson, J.D., Jurgens, R.F., Lau, E.L., Iii, M.A.S., and Schubert, G., 1996, Shape and Orientation of Mercury from Radar Ranging Data.:

Anzellini, S., Dewaele, A., Mezouar, M., Loubeyre, P., and Morard, G., 2013, Melting of Iron at Earth's Inner Core Boundary Based on Fast X-ray Diffraction: Science, v. 340, p. 464–466, doi:10.1126/science.1233514.

Bertka, C.M., and Fei, Y., 1998, Density profile of an SNC model Martian interior and the moment-of-inertia factor of Mars: v. 157, p. 79–88.

Bertka, C.M., and Fei, Y., 1997, Mineralogy of the Martian interior up to core-mantle boundary pressures: v. 102, p. 5251–5264.

Boccato, S., Torchio, R., Kantor, I., Morard, G., Anzellini, S., Giampaoli, R., Briggs, R., Smareglia, A., Irifune, T., and Pascarelli, S., 2017, The Melting Curve of Nickel Up to 100 GPa Explored by XAS: Journal of Geophysical Research: Solid Earth, v. 122, p. 9921–9930, doi:10.1002/2017JB014807.

Boehler, R., 1992, Melting of the FeFeO and the FeFeS systems at high pressure: Constraints on core temperatures: Earth and Planetary Science Letters, v. 111, p. 217–227, doi:https://doi.org/10.1016/0012-821X(92)90180-4.

Boehler, R., 1993, Temperatures in the Earth ' s core from melting-point measurements of iron at high static pressures f " T -: v. 363, p. 534–536.

Buono, A.S., and Walker, D., 2011, The Fe-rich liquidus in the Fe–FeS system from 1bar to 10GPa: Geochimica et Cosmochimica Acta, v. 75, p. 2072–2087, doi:https://doi.org/10.1016/j.gca.2011.01.030.

Chen, B., Li, J., and Hauck, S.A., 2008, Non-ideal liquidus curve in the Fe-S system and Mercury's snowing core: Geophysical Research Letters, v. 35, p. 10–14, doi:10.1029/2008GL033311.

Christensen, U.R., 2006, A deep dynamo generating Mercury’s magnetic field: Nature, v. 444, p. 1056–1058, doi:10.1038/nature05342.

Fei, Y., Bertka, C.M., and Finger, L.W., 1997, High-Pressure Iron-Sulfur Compound, Fe<sub>3</sub>S<sub>2</sub>;, and Melting Relations in the Fe-FeS System: Science, v. 275, p. 1621 LP – 1623, doi:10.1126/science.275.5306.1621.

Fei, Y., Li, J., Bertka, C.M., and Prewitt, C., 2000, Structure type and bulk modulus of Fe 3 S , a new iron-sulfur compound: v. 85, p. 1830–1833.

Gilfoy, F., and Li, J., 2020, Thermal state and solidification regime of the martian core: Insights from the melting behavior of FeNi-S at 20 GPa: Earth and Planetary Science Letters, v. 541, p. 116285, doi:https://doi.org/10.1016/j.epsl.2020.116285.

Hauck, S.A., Aurnou, J.M., and Dombard, A.J., 2006, Sulfur ’ s impact on core evolution and magnetic field generation on Ganymede: v. 111, p. 1–14, doi:10.1029/2005JE002557.

Hauck, S.A., Dombard, A.J., Phillips, R.J., and Solomon, S.C., 2004, Internal and tectonic evolution of Mercury: Earth and Planetary Science Letters, v. 222, p. 713–728, doi:https://doi.org/10.1016/j.epsl.2004.03.037.

Hauck II, S.A. et al., 2013, The curious case of Mercury’s internal structure: Journal of Geophysical Research: Planets, v. 118, p. 1204–1220, doi:10.1002/jgre.20091.

Hernlund, J., Leinenweber, K., Locke, D., and Tyburczy, J.A., 2006, A numerical model for steady-state temperature distributions in solid-medium high-pressure cell assemblies: American Mineralogist, v. 91, p. 295–305, doi:10.2138/am.2006.1938.

Hunten, D.M., and Sprague, A.L., 1997, Origin and character of the lunar and mercurian atmospheres: Advances in Space Research, v. 19, p. 1551–1560, doi:https://doi.org/10.1016/S0273-1177(97)00368-2.

Leinenweber, K., Tyburczy, J., Sharp, T., Soignard, E., Diedrich, T., Petuskey, W., Wang, Y., and Mosenfelder, J., 2012, Cell assemblies for reproducible multi-anvil experiments (the COMPRES assemblies): v. 97, p. 353–368.

Li J., and Agee C. B., The effect of pressure, temperature, oxygen fugacity and composition on partitioning of nickel and cobalt between liquid Fe-Ni-S alloy and liquid silicate: Implications for the Earth's core formation, *Geochim. Cosmochim. Acta* 65(11), 1821-1832 (2001).

Li, J., Hadidiacos, C., Mao, H.-K., Fei, Y., and Hemley, R.J., 2003, Behavior of thermocouples under high pressure in a multi-anvil apparatus: High Pressure Research, v. 23, p. 389–401, doi:10.1080/0895795031000088269.

Liu, J., and Li, J., 2019, Solidification of lunar core from melting experiments on the Fe–Ni–S system: Earth and Planetary Science Letters, doi:10.1016/j.epsl.2019.115834.

Malavergne, V., Toplis, M.J., Berthet, S., and Jones, J., 2010a, Highly reducing conditions during core formation on Mercury: Implications for internal structure and the origin of a magnetic field: Icarus, v. 206, p. 199–209, doi:10.1016/J.ICARUS.2009.09.001.

Malavergne, V., Toplis, M.J., Berthet, S., and Jones, J., 2010b, Highly reducing conditions during core formation on Mercury: Implications for internal structure and the origin of a magnetic field: Icarus, v. 206, p. 199–209, doi:https://doi.org/10.1016/j.icarus.2009.09.001.

Margot, J.L., Peale, S.J., Jurgens, R.F., Slade, M.A., and Holin, I. V, 2007, Large Longitude Libration of Mercury Reveals a Molten Core: , p. 710–715.

Morard, G., Andrault, D., Guignot, N., Siebert, J., Garbarino, G., and Antonangeli, D., 2011, Melting of Fe-Ni-Si and Fe-Ni-S alloys at megabar pressures: Implications for the core-mantle boundary temperature: Physics and Chemistry of Minerals, v. 38, p. 767–776, doi:10.1007/s00269-011-0449-9.

Mori, Y., Ozawa, H., Hirose, K., Sinmyo, R., Tateno, S., Morard, G., and Ohishi, Y., 2017, Melting experiments on Fe – Fe 3 S system to 254 GPa: v. 464, p. 135–141, doi:10.1016/j.epsl.2017.02.021.

Ness, N.F., Behannon, K.W., Lepping, R.P., and Whang, Y.C., 1976, Observations of Mercury's magnetic field: Icarus, v. 28, p. 479–488, doi:https://doi.org/10.1016/0019-1035(76)90121-4.

Ness, N.F., Behannon, K.W., Lepping, R.P., and Whang, Y.C., 1975, The magnetic field of Mercury, 1: Journal of Geophysical Research (1896-1977), v. 80, p. 2708–2716, doi:10.1029/JA080i019p02708.

Ness, N.F., Behannon, K.W., Lepping, R.P., Whang, Y.C., and Schatten, K.H., 1974, Magnetic Field Observations near Mercury: Preliminary Results from Mariner 10: Science, v. 185, p. 151 LP – 160, doi:10.1126/science.185.4146.151.

Pommier, A., Laurenz, V., Davis, C., and Frost, D., 2018, Melting Phase Relations in the Fe-S and Fe-S-O systems at core conditions in small terrestrial bodies: Icarus, v. 306, p. 150–162, doi:10.1016/j.icarus.2018.01.021.

Riner, M.A., Bina, C.R., Robinson, M.S., and Desch, S.J., 2008, Internal structure of Mercury: Implications of a molten core: Journal of Geophysical Research: Planets, v. 113, doi:10.1029/2007JE002993.

Shen, G., Mao, H., Hemley, R.J., Duffy, T.S., and Rivers, M.L., 1998, Melting and crystal structure of iron at high pressures and temperatures: Geophysical Research Letters, v. 25, p. 373–376, doi:10.1029/97GL03776.

Stevenson, D.J., Spohn, T., and Schubert, G., 1983, Magnetism and thermal evolution of the terrestrial planets: Icarus, v. 54, p. 466–489, doi:https://doi.org/10.1016/0019-1035(83)90241-

5.

Stewart, A.J., Schmidt, M.W., Westrenen, W. Van, and Liebske, C., 2007, Mars: A New Core-Crystallization Regime: v. 316, p. 1323–1326, doi:10.1126/science.1140549.

Turcotte., G., and Schubert., D.L., 2002, Geodynamics: Cambridge University Press, v. 40, p. 246, doi:10.1002/gj.987.

Vilim, R., Stanley, S., and Hauck II, S.A., 2010, Iron snow zones as a mechanism for generating Mercury's weak observed magnetic field: Journal of Geophysical Research: Planets, v. 115, doi:10.1029/2009JE003528.

Williams, Q., 2009, Bottom-up versus top-down solidification of the cores of small solar system bodies : Constraints on paradoxical cores: Earth and Planetary Science Letters, v. 284, p. 564–569, doi:10.1016/j.epsl.2009.05.019.

Zhang, L., and Fei, Y., 2008, Effect of Ni on Fe – FeS phase relations at high pressure and high temperature: v. 268, p. 212–218, doi:10.1016/j.epsl.2008.01.028.

Zhang, D., Jackson, J.M., Zhao, J., Sturhahn, W., Alp, E.E., Hu, M.Y., Toellner, T.S., Murphy, C.A., and Prakapenka, V.B., 2016, Temperature of Earth's core constrained from melting of Fe and Fe0.9Ni0.1 at high pressures: Earth and Planetary Science Letters, v. 447, p. 72–83, doi:https://doi.org/10.1016/j.epsl.2016.04.026.

Zurbuchen, T.H., Raines, J.M., Gloeckler, G., Krimigis, S.M., Slavin, J.A., Koehn, P.L., Killen, R.M., Sprague, A.L., McNutt, R.L., and Solomon, S.C., 2008, MESSENGER observations of the composition of mercury's ionized exosphere and plasma environment: Science, v. 321, p. 90–92, doi:10.1126/science.1159314.